AGU PUBLICATIONS

JGR

Journal of Geophysical Research: Oceans

RESEARCH ARTICLE

10.1002/2015JC011600

Key Points:
- Wind pulses associated with a developing MJO event generated NIWs at 8°S in the Indian Ocean
- The energy flux of NIWs in the pycnocline is 30–40% of the wind input to the ML
- A critical level in the pycnocline dissipated 20% of the wave energy

Supporting Information:
- Supporting Information S1
- Figure S1
- Figure S2
- Figure S3
- Figure S4
- Figure S5
- Figure S6
- Figure S7
- Figure S8
- Figure S9
- Figure S10
- Figure S11
- Figure S12
- Figure S13
- Figure S14

Correspondence to:
S. M. Soares,
saulo@hawaii.edu

Citation:
Soares, S. M., A. Natarov, and K. J. Richards (2016), Internal swells in the tropics: Near-inertial wave energy fluxes and dissipation during CINDY, *J. Geophys. Res. Oceans*, *121*, 3297–3324, doi:10.1002/2015JC011600.

Received 28 DEC 2015
Accepted 18 APR 2016
Accepted article online 21 APR 2016
Published online 20 MAY 2016

Internal swells in the tropics: Near-inertial wave energy fluxes and dissipation during CINDY

S. M. Soares[1,2], A. Natarov[2], and K. J. Richards[1,2]

[1]Department of Oceanography, University of Hawai'i at Mānoa, Honolulu, Hawaii, USA, [2]International Pacific Research Center, University of Hawai'i at Mānoa, Honolulu, Hawaii, USA

Abstract A developing MJO event in the tropical Indian Ocean triggered wind disturbances that generated inertial oscillations in the surface mixed layer. Subsequent radiation of near-inertial waves below the mixed layer produced strong turbulence in the pycnocline. Linear plane wave dynamics and spectral analysis are used to explain these observations, with the ultimate goal of estimating the wave energy flux in relation to both the energy input by the wind and the dissipation by turbulence. The results indicate that the wave packets carry approximately 30–40% of the wind input of inertial kinetic energy, and propagate in an environment conducive to the occurrence of a critical level set up by a combination of vertical gradients in background relative vorticity and Doppler shifting of wave frequency. Turbulent kinetic energy dissipation measurements demonstrate that the waves lose energy as they propagate in the transition layer as well as in the pycnocline, where approaching this critical level may have dissipated approximately 20% of the wave packet energy in a single event. Our analysis, therefore, supports the notion that appreciable amounts of wind-induced inertial kinetic energy escape the surface boundary layer into the interior. However, a large fraction of wave energy is dissipated within the pycnocline, limiting its penetration into the abyssal ocean.

1. Introduction

Internal swells are groups or packets of near-inertial internal waves (NIW) generated by surface mixed layer (ML) inertial oscillations that propagate into the ocean interior [*Alford*, 2001]. Inertial oscillations, motions at or very near the local inertial frequency $f_\circ$, are an integral part of the oceanic response to wind forcing and contain a large fraction of the work done by the wind on the surface ML currents [*Pollard and Millard Jr*, 1970; *D'Asaro*, 1985]. The decay of ML inertial oscillations is a complex process that involves the radiation of NIW packets and shear-driven turbulent mixing at the base of the ML [*D'Asaro*, 1989; *Plueddemann and Farrar*, 2006; *Soares and Richards*, 2013]. Depending on the preferential decay path, the wind-induced inertial kinetic energy (IKE) takes, its ultimate dissipation will occur either locally via turbulent mixing near the base of the surface ML or remotely in the pycnocline or deep ocean. Climate is sensitive to the IKE fueled ocean mixing [*Jochum et al*., 2013], but because NIWs are not well resolved by typical ocean general circulation models (OGCM), their contribution needs to be parameterized.

It is still unclear what fraction of the wind work on inertial currents (see estimates by *Watanabe and Hibiya* [2002]; *Alford* [2003]; *Jiang et al*. [2005]) is emitted as internal swells versus locally dissipated at the ML base. Some numerical modeling studies with global and regional OGCMs suggest that, in midlatitudes, at most 20% of the wind input of IKE to the ML propagates below the surface boundary layer [*Furuichi et al*., 2008; *Zhai et al*., 2009]. In contrast, *Soares and Richards* [2013] show that in the tropical eastern Pacific a larger fraction can escape the boundary layer. Due to their strong upper ocean stratification, tropical regions may be hotspots for NIW activity.

Data collected during the DYNAMO/CINDY2011 field campaign (hereafter referred as CINDY) in the tropical Indian Ocean provide a rare opportunity to derive estimates of energy fluxes and wave energy dissipation from direct in situ observations and relate them to the local wind input. The goal of the CINDY project was to study air-sea interactions at intraseasonal timescales, particularly the developing stages of atmospheric convective disturbances such as the Madden Julian Oscillation (MJO) [*Yoneyama et al*., 2013]. During the beginning of the first leg of the CINDY observations, a convective disturbance propagated over the R/V *Mirai* (Figures 1a and 1b), triggering inertial oscillations in the ML and subsequent NIW radiation in the

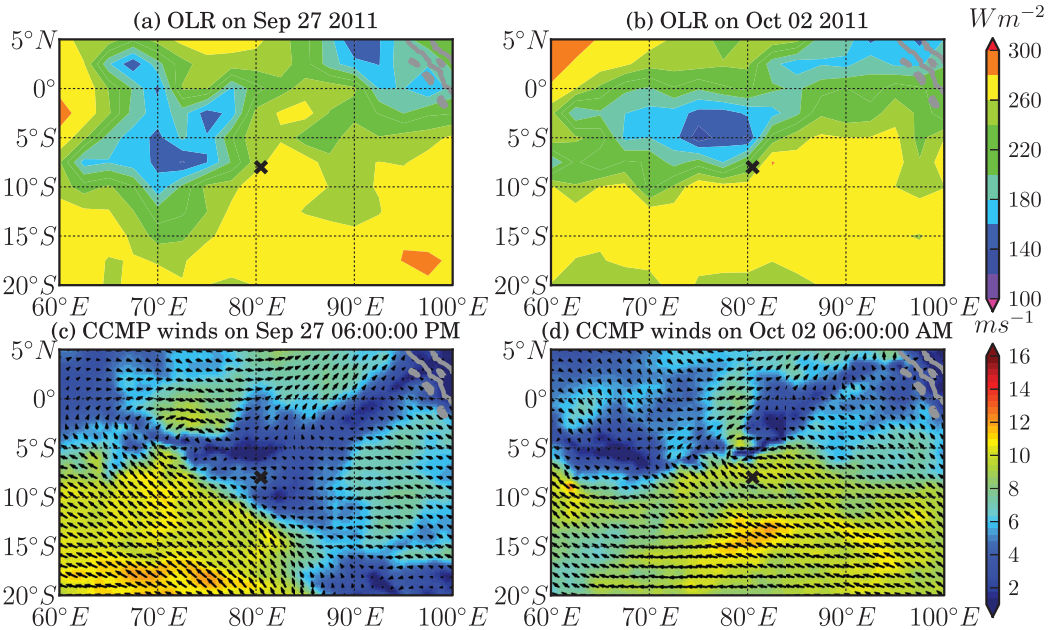

Figure 1. Maps of the study area with a black cross marking the location of the R/V *Mirai* station at 8°S, 80.5°E. Top maps show Outgoing Long Wave radiation (OLR) (a) 3 days prior to the sampling period at the station and (b) 3 days after the start of the sampling period. The approximate OLR threshold that defines deep convection is 180 Wm^{-2}. Bottom maps show 10 m surface winds (c) 3 days prior to the sampling period and (d) 3 days after the start of the sampling period. Arrows represent wind vectors while the shading represents wind speed magnitude.

thermocline. Additionally, another NIW packet is observed at depth in association with elevated dissipation rates.

In this paper, we estimate the fraction of wind-induced inertial energy fluxed downward by the radiating internal waves, and study their propagation and dissipation. Results of the various analyses indicate that up to 40% of the wind input of IKE to ML is radiated downward into the ocean interior and that significant loss of NIW energy occurs within the seasonal pycnocline.

First we describe the data used in this study (section 2), followed by short descriptions of the atmospheric forcing episode (section 3) that triggered the ML inertial oscillations and of the background oceanic conditions relevant to the dynamics of near-inertial motions (section 4). In section 5, we analyze the ML inertial response and estimate the flux of IKE from the winds to the oceanic mixed layer. Section 6 describes the methods and results of the NIW packet analysis, as well as of ray tracing and energy budget calculations. Section 7 contains the discussion and concluding remarks.

2. Data

Data used in this study consists of in situ, remote, and numerical model output data sets of ocean and meteorological variables. The in situ observations allow a detailed examination of vertical and temporal aspects, while the ancillary data sets, remote satellite data, and model output data, permit investigation of the horizontal structure of atmospheric and oceanic background conditions that occurred during the in situ collection.

The in situ data consists of measurements made aboard the R/V *Mirai* during the CINDY cruise as part of an international MJO investigation field campaign [see *Yoneyama et al.*, 2013 for details] at a single station at 8°S 80.5°E (Figure 1) from 28 September to 26 October 2011. Lowered acoustic Doppler current profiler (LADCP) and conductivity temperature depth (CTD) casts down to 500 m were conducted approximately every 3 h. In between LADCP-CTD casts, one to three Micro-Structure Profiler (MSP) casts were also performed in order to measure the turbulent kinetic energy dissipation rate (ϵ). The 600 kHz LADCP data were binned into $\approx$2 db depth bins, while the post processed CTD data were binned in 1 db bins. The R/V *Mirai* was also equipped with a hull mounted 75 kHz *Ocean Surveyor* acoustic Doppler current profiler (SADCP), which was post processed for quality yielding

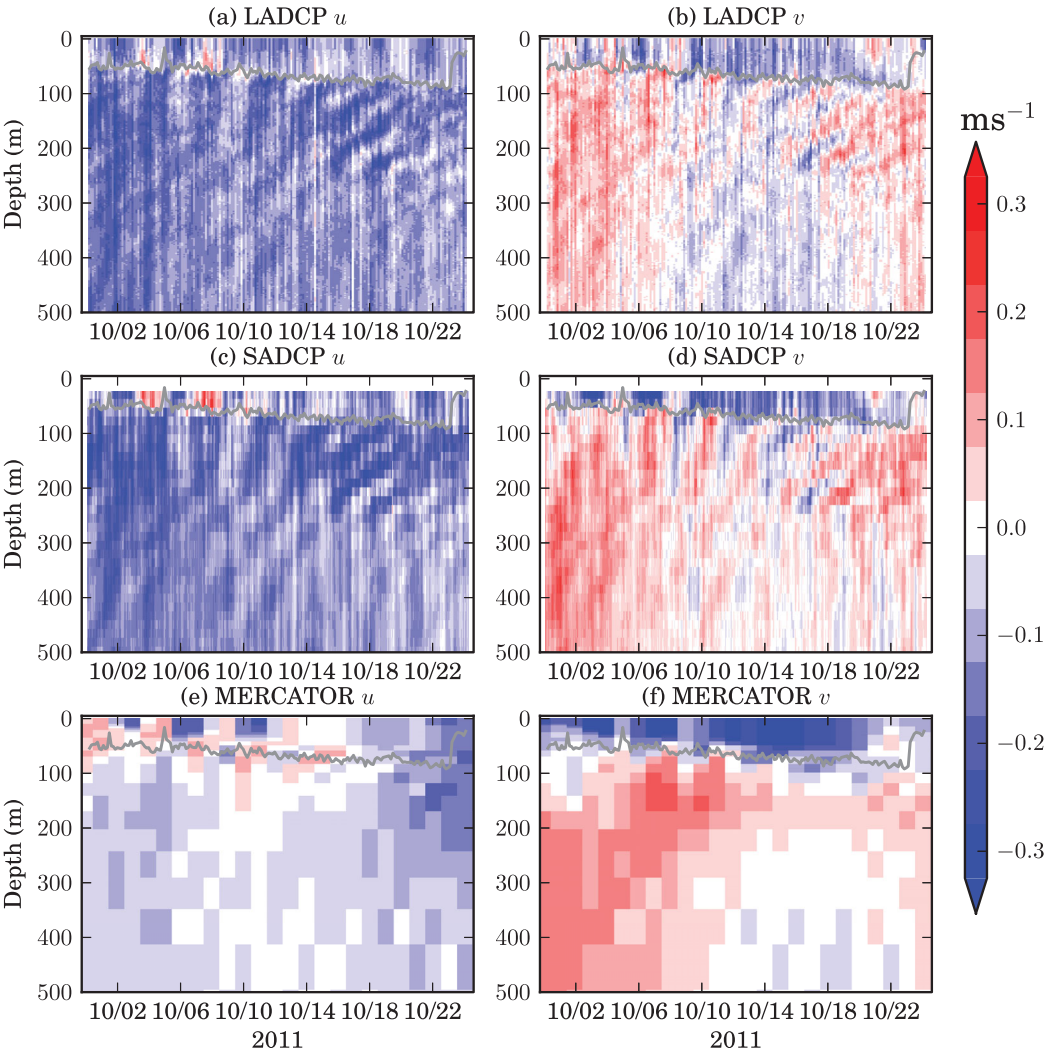

Figure 2. (top) LADCP *u* (a) and *v* (b) current components collected during CINDY at 8°S, 80.5°E. (middle) the SADCP *u* (c) and *v* (d) current components. (bottom) the *u* (e) and *v* (f) current components obtained from MERCATOR output at 8°S, 80.5°E. The dark-grey line is the ML depth.

a vertical resolution of 16 m, with a range down to 700 m and a temporal resolution of 5 min. Following *Alford and Gregg* [2001], we produced 30 min bin averages of SADCP data to reduce noise. These observations are presented on Figures 2a–2d and 3a–b. From the CTD potential density (ρ, Figure 3a) data, we compute a ML depth as the depth where ρ exceeds its surface value (taken as the upper 5 m average ρ) by 0.125 kgm^{-3}. This ML depth estimate corresponds well with both the base of the deepest mixing layers seen in the ϵ data (Figure 3b) and with the top of the strongly stratified layer in the upper pycnocline that inhibits surface forcing, implying this definition is appropriate for our study (we note that a smaller density jump produces a ML depth that closely follows the active mixing depth). Winds were measured at 6 s interval by the anemometer array on the foremast of the R/V *Mirai* (24 m height), then post processed to 10 min averages and converted to a 10 m height wind estimate. Winds were further averaged to 30 min bins to reduce noise and the COARE algorithm version 3.0 [*Fairall et al.*, 2003] was used to compute stresses relative to the surface currents (taken as the uppermost SADCP bin).

Oceanographic remote sensing data consists of upper ocean absolute geostrophic currents from the Archiving, Validation, and Interpretation of Satellite Oceanographic data (AVISO) delayed time product available on a 1/4° grid at weekly intervals. We also use the Ocean Surface Oceanographic Current Analysis-Real Time (OSCAR) pentad product available on a 1/3° grid, which contains both wind-driven Ekman currents and

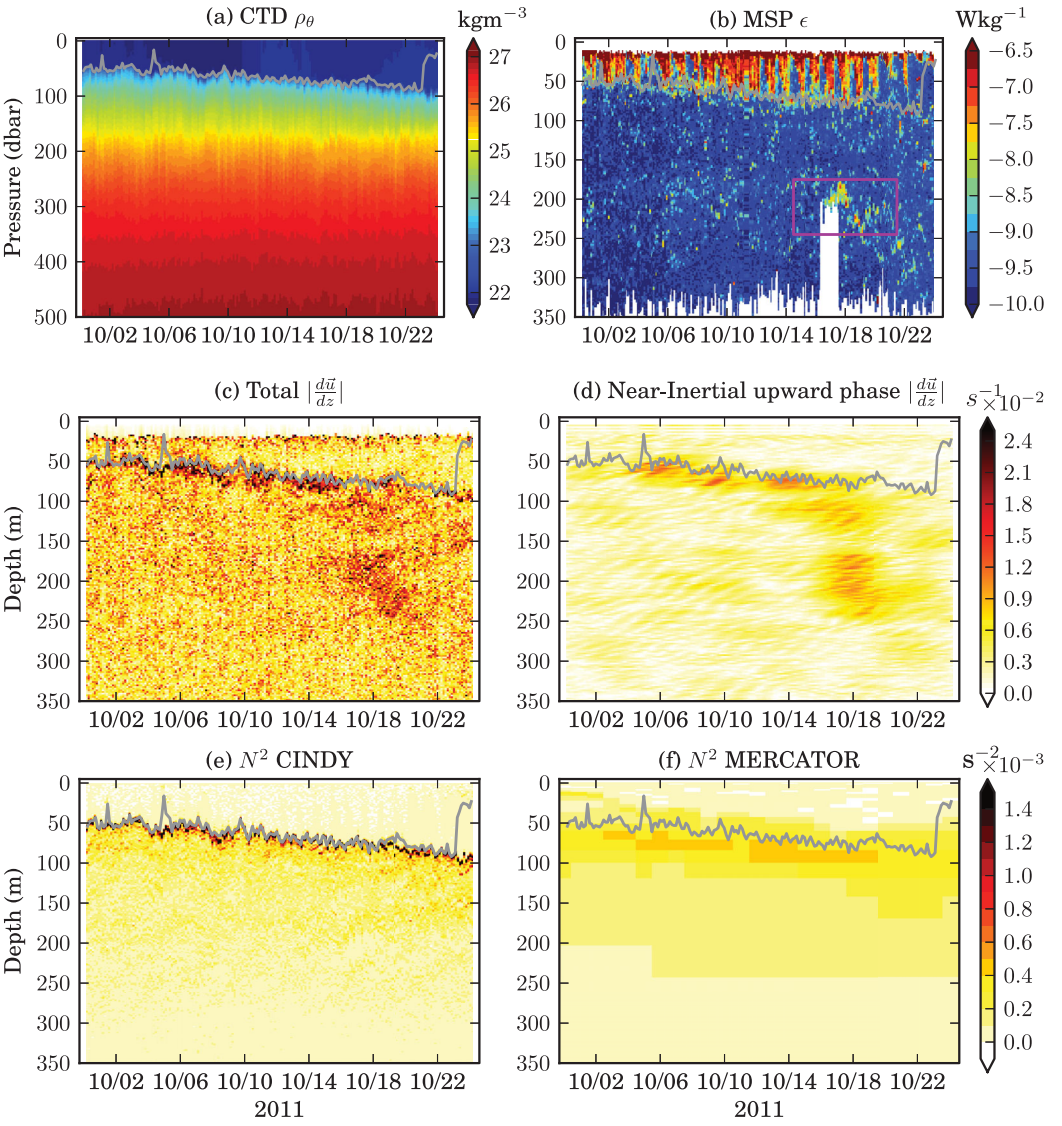

Figure 3. (a) Potential density (σ_θ) at contour intervals of 0.125 kgm^{-3}. (b) Base 10 logarithm of the Turbulent Kinetic Energy (TKE) dissipation rate (ϵ). (c) Current shear magnitude ($|\frac{d\vec{u}}{dz}|$) and (d) the 2–6 days band-passed upward-phase-propagating current shear magnitude derived from LADCP measurements. Buoyancy frequency squared (N^2) computed from (e) in situ density data and (f) from MERCATOR density output at 8°S, 80.5°E.

geostrophic currents [*Bonjean and Lagerloef*, 2002]. These data are used in section 3 to construct spatial maps of the background ocean conditions in the area and to assist in evaluating a model skill.

For remote meteorological data, we use satellite-derived outgoing longwave radiation (OLR) and 10 m winds from the Cross-Calibrated Multi-Platform Ocean Surface Wind Vector Analyses (CCMP). CCMP is a blended analysis product between several satellite data sources and European Centre of Medium-Range Weather Forecasts (ECMWF) ERA-I reanalysis [*Atlas et al.*, 2011]. These data are used to describe the atmospheric forcing prior and during the CINDY cruise.

Output from the MERCATOR OCEAN global analysis is used to construct three-dimensional maps of stratification and currents of the study area. MERCATOR is based on OPA (Océan PArallélisé), a *z*-coordinate primitive equation model that assimilates satellite sea surface temperature (SST) and sea surface height anomalies (SSH) along with available in situ temperature and salinity from ship-borne sensors, drifters, moorings, and CTD and expendable bathythermograph (XBT) casts. Atmospheric forcing for this version of MERCATOR-OPA is from daily-averaged ECMWF operational forecasts. Output is available as daily averages

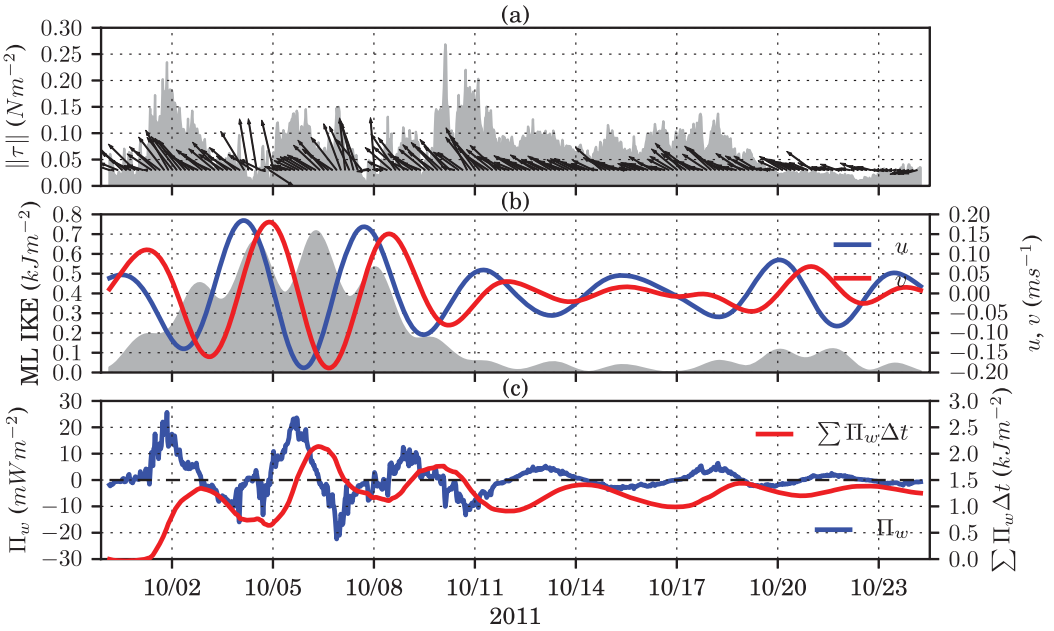

Figure 4. (a) Wind stress magnitude (shaded) with unit arrows indicating wind direction. (b) Inertial Kinetic Energy (IKE) in the ML (shaded) and SADCP demodulated inertial current components at 30 m depth. (c) Wind work on ML inertial currents and the accumulated wind work.

at a 1/12° horizontal resolution grid and a total of 50 vertical levels, of which 29 are in the upper 300 m, yielding vertical resolutions varying from 1 m near the surface, to 20–50 m below 100 m and to 400 m near the bottom. Model zonal velocity u, meridional velocity v, and N^2 (buoyancy frequency squared) fields are shown in bottom plots of Figures 2 and 3. MERCATOR output is also used to evaluate vorticity estimates derived from the NIW packet analysis and as background conditions for the three-dimensional ray tracing experiments.

3. Atmospheric Forcing

A large convection area, marked by the low values of OLR in Figure 1a, is seen west of the CINDY station on 27 September accompanied by a large area of weak winds east of its center and over the CINDY station location (Figure 1c). Just prior to the sampling period and during its early stages, this convective activity was driven by both the developing dry phase of an MJO event as well as eastward propagating convective coupled Kelvin waves [*Gottschalck et al.*, 2013]. After 27 September, the convection area west of the R/V *Mirai*'s position appears to break apart as it spreads eastward, weakening the wind during the first day and a half of the sampling period (Figure 4a). Between 1 and 2 October, a center of deep convection (large negative OLR anomalies) quickly develops just northwest of the station (Figure 1) triggering an onset of SE winds over the area (Figure 1d). As this deep convection center moves northeast on the next 2 days, the SE winds weaken once again. During the following week (4–11 October), convective variability in the area seems to be related to the wind pulses measured by the ship's anemometer (Figure 4a). After 11 October, the SE winds resume for about 10 days (Figure 4a). Around 20 October, convection due to the developing wet phase of the MJO brings about another weakening of the winds in the area. More detailed discussions about the meteorological conditions during all of the DYNAMO/CINDY2011 campaign can be found in *Yoneyama et al.* [2013]; *Gottschalck et al.* [2013]; *Shinoda et al.* [2013]; and *Seiki et al.* [2013].

4. Background Upper Ocean Conditions

We define "background" as the variability with timescales longer than about four local inertial periods (IPs, of $\approx$ 3.6 days). In terms of circulation, we are primarily interested in vorticity (ζ) and mean

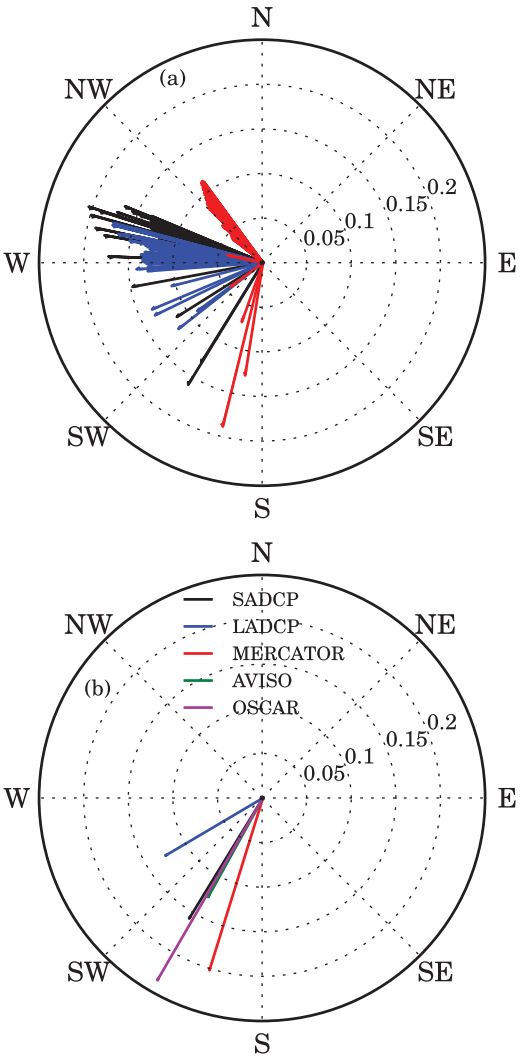

Figure 5. (a) Current vectors, averaged over the sampling period, from the surface down to 500 m for LADCP (blue, 2 m interval), SADCP (black, 16 m interval), and MERCATOR (red, 16 m interval). (b) Near-surface current vectors averaged over the sampling period. The LADCP and SADCP in situ currents (averaged over upper 45 m and at 30 m depth, respectively) are compared with MERCATOR (averaged over upper 45 m), AVISO and OSCAR products (at 15 m depth).

currents, secondarily in lateral strain rates (i.e., normal and shear strain rates, S_n and S_s, respectively) and divergence (δ) since these properties impact the dynamics of near-inertial motions (see Appendix A for definitions).

In the beginning of the sampling period, we observe a ≈40 m deep ML over a sharp, strongly stratified 30–40 m thick transition layer (TL) [*Dohan and Davis*, 2011] at the top of the pycnocline (Figures 3e and 3a). Throughout the record, the ML and TL exhibit a deepening trend. As the TL deepens, its thickness remains constant but its stratification weakens and diffuses, while the stratification within the pycnocline strengthens. These changes coincide with the arrival of a positive SSH anomaly signal [*Seiki et al*., 2013]. The variability in stratification is mostly captured by MERCATOR (Figure 3f), particularly the deepening trend of both the ML and TL, although the TL in the model is substantially broader and weaker than observed.

According to *Seiki et al*. [2013], during most of the sampling period, the R/V *Mirai* was located on the northern half of a Rossby wave gyre (e.g., Figures 7a and 7c), resulting in southwest mean surface currents as observed in situ (Figure 5b) and in OSCAR and AVISO. The background currents veer W-NW with depth and are directed W-SW in the TL and ML (Figure 5a). Because changes in background currents are small during the sampling record (Figure 2), we use time mean currents in our analyses. MERCATOR output differs from observations in high-frequency variability, but represents the observed mean currents reasonably well (compare Figures 2a–2d with 2e and 2f).

Time series of ζ, δ, S_n, and S_s at the station location are shown in Figure 6. Anticyclonic vorticity develops near the surface over the first week of sampling (Figure 6a), and is consistent with the Rossby gyre pattern (Figures 7a, 7c, and 7e) and the deepening of the ML. In contrast, divergence is very weak, consistent with a quasi-geostrophic background flow field, while the dominant vorticity and strain rates are consistent with the existence of a vigorous mesoscale eddying field as depicted in Figure 7. The relative contribution of each term is consistent among all products depicted in Figure 6, although MERCATOR output shows increased short timescale variability, larger amplitudes, and different timings of signal arrivals. Vorticity from depth levels beneath 100 m and 200 m (the lighter grey lines in Figure 6a) suggest a two-layered system during the sampling period, with predominant anticyclonic vorticity near the surface and cyclonic vorticity beneath 100 m. MERCATOR shows more filaments and small-scale eddies associated with the main Rossby wave feature than AVISO and OSCAR vorticity maps (Figure 7). These smaller-scale features produce the localized high-frequency vorticity and strain oscillations seen in Figure 6. Given the

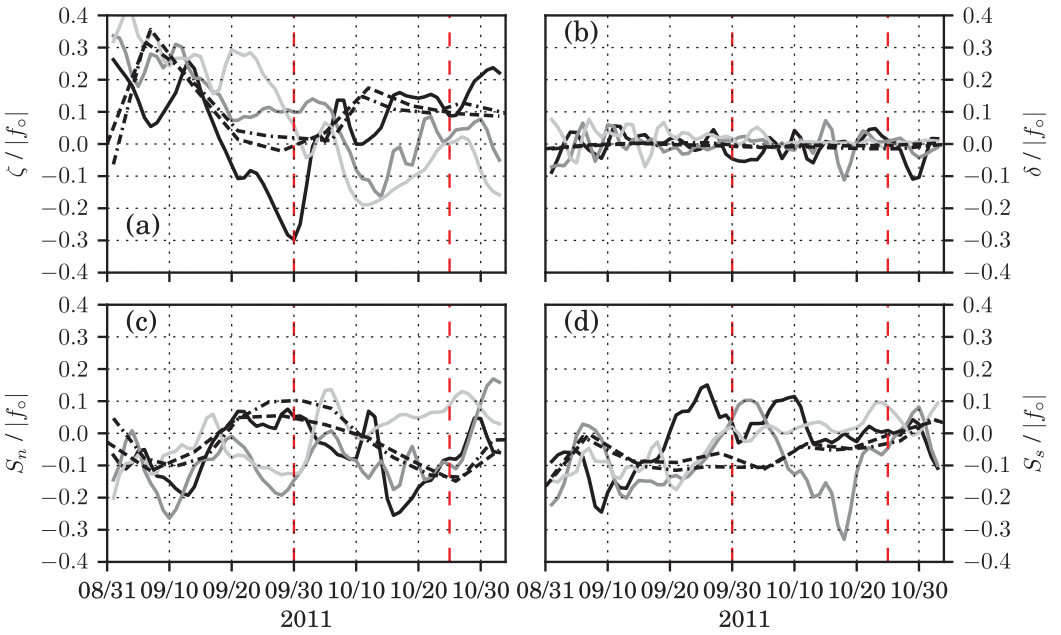

Figure 6. Time-series of (a) vorticity, (b) divergence, (c) normal component of the horizontal strain, and (d) shear component of the horizontal strain at 8°S, 80.5°E. Dashed lines are for AVISO-derived quantities, dashed dotted lines for OSCAR, and solid lines are for 7 days low-passed MERCATOR at select depths (black: 15 m, darker grey: 110 m and light grey: 220 m). Red vertical-dashed lines mark the beginning and end of the sampling period.

reasonable model-satellite product agreement, we deem MERCATOR output to be satisfactory to provide the background conditions for our analysis of near-inertial motions.

Note that vorticity in the layers appears to change sign in the model around 10 October (solid lines in Figure 6a). It seems reasonable to construct a scenario where neutral to weak anticyclonic vorticity dominates the surface ML while stronger AC vorticity dominates the TL and pycnocline prior to and during the first few days of the sampling period. The propagation of the Rossby wave over the station steadily deepens the ML and TL (with the latter weakening while increasing the stratification in the pycnocline, see Figure 3e), and induces the surface vorticity to rotate anticyclonically, with this pattern dominating from the surface down to about 100–150 m depth, below which vorticity is cyclonic.

5. Inertial Oscillations in the Mixed Layer

5.1. Dynamics

During the first 10 days of October the winds pulsated on and off, generating inertial oscillations in the ML, as seen in the demodulated current time series (Figure 4b). The spectrum of ML currents shows a peak at 0.92 $f_\circ$ (Figure 8a; $f_\circ$ is the local inertial frequency at 8°S), albeit with substantial bandwidth. A dispersion relation for ML motions indicates that inertial oscillations in the absence of strong background divergence and strain rates should have a frequency $\omega_\circ$ equal to f_{eff}, the effective inertial frequency [see e.g., *Chavanne et al.*, 2012]. The subinertial peak frequency suggests that anticyclonic background relative vorticity dominates during the first three IPs, in agreement with both MERCATOR and AVISO/OSCAR vorticity shown in Figure 6a.

Figure 8b shows the near-inertial current ellipses, obtained via complex demodulation of SADCP currents at the peak frequency reported above. The ellipses are tilted SW-NE, roughly the same orientation of the wind disturbance front (see Figure 1d), with a major to minor axis ratio r_2 of 1.36–1.47. The *u* and *v* polarization relations, specifically the eccentricity of inertial current ellipses, can be used to provide an estimate of the background horizontal shear along the direction of the orientation of the inertial current ellipses (given by its major-axis, see details and notation in Appendix A), assuming that ML inertial oscillations are not Doppler shifted. This is a reasonable approximation since the ML inertial oscillations are expected to have large horizontal scales, judging from the large-scale pattern of the wind forcing (Figure 1d). Letting x^r and y^r be

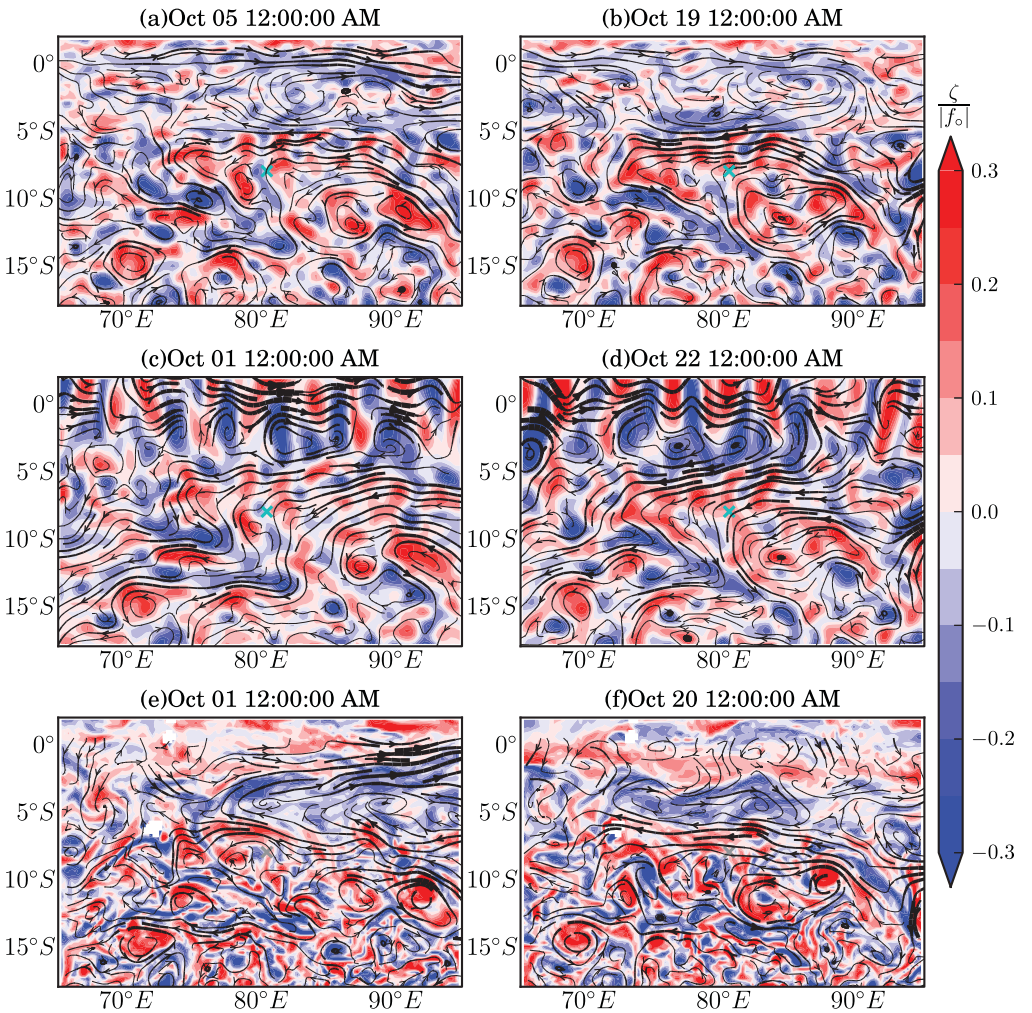

Figure 7. Maps of near-surface vorticity ζ (shading) and circulation (lines). (top) Obtained from AVISO absolute geostrophic currents nearest the (a) beginning and (b) end of the sampling period. (middle) From OSCAR currents nearest the (c) beginning and (d) end of the sampling period. (bottom) Obtained from MERCATOR currents averaged in upper 45 m for the (e) beginning and (f) for the end of the sampling period. Crosses mark the location of the R/V *Mirai* station at 8°S, 80.5°E. Thickest lines denote flows in excess of 1 ms^{-1}.

coordinates oriented along the ellipse semimajor and semiminor axes, respectively, and letting U^r and V^r be, respectively, the along-major-axis and cross-major-axis components of the background velocity, the calculated along major-axis shear of the cross-major-axis component of velocity, $V^r_{x^r}$, is $-0.35\ f_\circ$. The background vorticity is therefore anticyclonic if the background is either in solid body rotation (in which case $f_{\text{eff}} = -0.65\ f_\circ$), or is a parallel shear flow with no $U^r_{y^r}$ (where $f_{\text{eff}} = -0.82\ f_\circ$). Although the sign of the ML background vorticity is in agreement with ancillary data, the magnitude of f_{eff} estimates based on solid body rotation or parallel shear flow are much higher (e.g., compare to supporting information Figure S1a). If indeed $f_{\text{eff}} = \omega_\circ = 0.92 f_\circ$, then $U^r_{yr} = -0.3 f_\circ$, implying that assumptions of solid body rotation or parallel shear flow are likely invalid. Horizontal shears of this magnitude, however, are not uncommon in the MERCATOR eddy field (Figure 7e).

Although the analysis above takes into account the background current, it ignores the forced-damped aspects of the ML inertial system. Note that the major axis of the observed inertial ellipse (blue line in Figure 8b) is oriented nearly perpendicular to the dominant orientation of wind forcing (e.g., the stronger SE wind bursts of Figure 4a), suggesting an influence of Ekman dynamics and implying that the Ekman transport in the ML has near-inertial variability. This near-inertial variability in Ekman transport likely originates from the timing of the bursts (approximately 4 days apart, in Figure 4a).

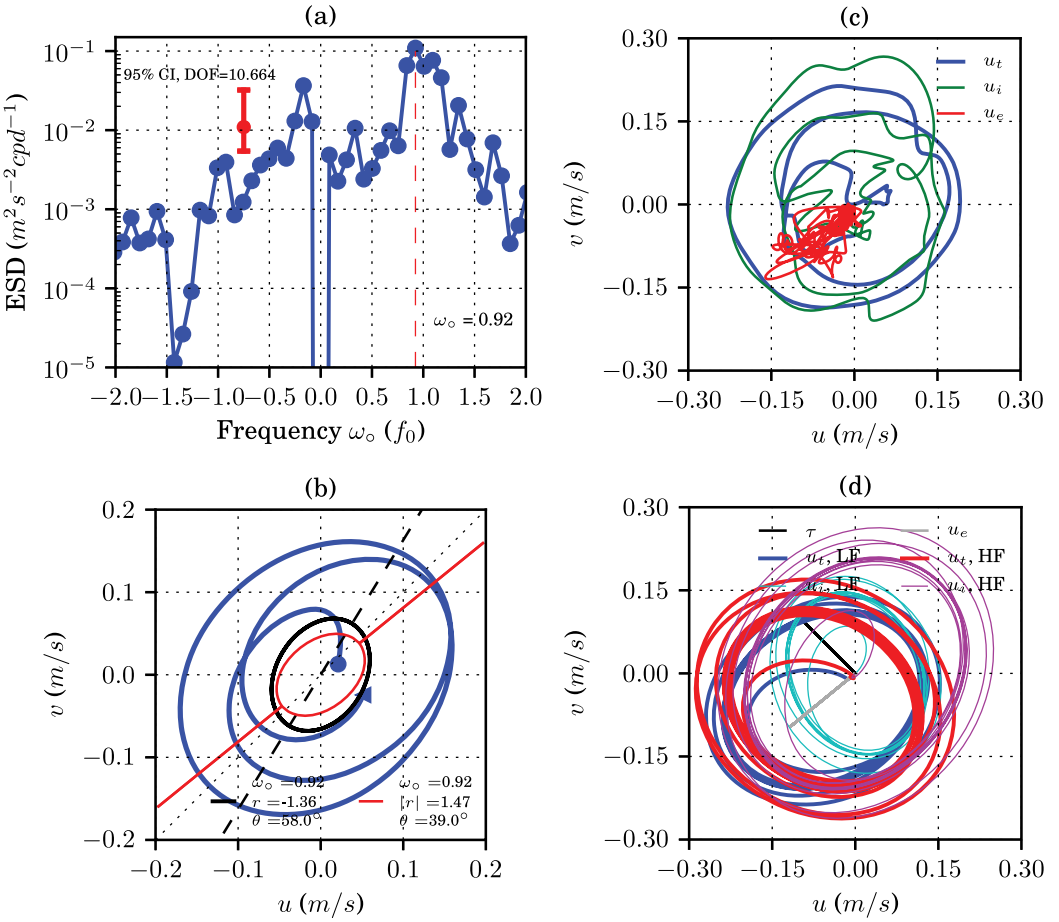

Figure 8. (a) Rotary spectrum for mixed layer currents from SADCP measurements. (b) Mixed layer current ellipse during the first three inertial periods (≈11 days) at 8°S, 80.5°E. Also shown are the inertial oscillation ellipses and its parameters obtained from the FFT (red) and HM94 (black, dashed line shows the major axis) methods. (c) Current ellipses for slab-model solutions (u_e, u_i, u_t) forced by observed wind stress and ML depth, using r_d^{-1} = 5.75 days. (d) Ellipses for slab-model solutions forced with idealized SE wind bursts, constant ML depth: HF where pulses have a frequency 20% above $f_\circ$ and LF with frequency 20% below $f_\circ$.

We demonstrate how Ekman currents influence near-inertial ellipses by examining solutions of a slab ML model (see formulation in *D'Asaro* [1985]), where the Ekman (u_e) and inertial (u_i) components of the solution are readily separable. We discuss two types of solutions. First the slab-model is forced with winds measured aboard the ship to address whether the observed ellipse can result from the combination of locally forced Ekman and inertial components. Then a series of experiments with idealized SE wind pulses is used to investigate the behavior of the ellipses as a function of the frequency of the pulses.

Current hodographs from the slab-model solutions forced by observed winds are shown in Figure 8c, using a damping coefficient r_d which yields a best-fit between model and data. The model u_i ellipse shows eccentricity with a major-axis orientation roughly in the north-south direction. This eccentricity arises because of time varying work done on the inertial currents by the winds. The ellipse traced by the total currents $u_t = u_e + u_i$ on the other hand, albeit less eccentric, has a similar tilt as observed (NE-SW oriented). Given that one observes u_t, the impact of the Ekman currents with frequency close to inertial is difficult to disentangle using frequency-filtering techniques. The weaker eccentricity in model currents relative to observed currents suggests that background current shears still contributed significantly to the observed near-inertial ellipse.

Hodographs from experiments with forcing frequency at 0.2 $f_\circ$ and 1.2 $f_\circ$, termed LF and HF, respectively, are shown in Figure 8d. The curves for experiment LF show an inertial ellipse oriented nearly parallel to the wind and total ellipse oriented parallel to the Ekman transport, while the reverse occurs in the HF

experiment. From these experiments, it is clear that the primary effect of the Ekman currents is to shift the phase of the near-inertial motions, rotating the ellipse. All eccentricity resides in the inertial component and is induced by the wind-work. A pattern is evident from the pool of experiments: when the forcing frequency is less than $f_\circ$ the inertial ellipse is aligned with the wind, while the total-current ellipse tilts perpendicular to the wind; when the forcing frequency is greater than $f_\circ$, the pattern is reversed. This is consistent with the observations, as we estimate the dominant forcing frequency to be slightly lower than $f_\circ$, hence why the ellipse of Figure 8b is aligned with the Ekman transport.

Based on these results, both local forcing and background shears appear to contribute to the observed ellipse orientation and eccentricity, since each process alone results either in too little eccentricity (forcing) or too strong background current shears. Interestingly, the slab-model solutions forced by real winds possess a subinertial peak-frequency, suggesting that the observed subinertial peak arises from the forcing rather than the background vorticity. But the effects of forcing and background flow are not mutually exclusive, since low-frequency forcing over a cyclonic background would likely result in more negative wind work, producing decaying oscillations rather than the growing ones we observed. An additional important outcome, with implications to the analysis of NIWs, is that the assumption of solid body rotation leads to overestimation of the magnitudes of background shears (when these are considered alone) and hence of f_{eff} estimates.

5.2. Energetics

The observed pulse-like wind variability translated to a positive wind work on ML inertial currents for the first two IPs (Figure 4c), when the ML IKE reaches its peak on 6 October. Afterward, when inertial currents and wind pulses go out of phase, the wind work becomes negative and the ML IKE quickly decreases.

The amount of IKE in the ML is significantly less than reported by *Cuypers et al*. [2013] following an Indian Ocean tropical storm, but is comparable to typical inertial oscillations reported by *Soares and Richards* [2013] in the eastern tropical Pacific. With inertial current root mean square (RMS) speeds near 0.2 ms^{-1}, the IKE in the ML during CINDY is clearly well above background levels (Figure 4b), as maximum wind IKE inputs estimated during CINDY barely reach 20 mWm^{-2}, while peak IKE input observed by *Cuypers et al*. [2013] are 50% higher as a consequence of higher wind stress magnitudes.

The wind work on the ML inertial oscillations or the flux of IKE from the winds is on average $\approx$4.1 mWm^{-2} up to the time of the IKE peak in the ML (Figure 4c). Averaged over the period to when the IKE returns to background levels, about three IPs since record start, the flux is much lower at 1.1–1.4 mWm^{-2}, in part due to the wind forcing as pointed out above. The energy flux may be slightly overestimated because we are neglecting the ML deepening that occurred. Since the ancillary data suggests that the background strain field contribution on f_{eff} is negligible (supporting information Figure S1b), we assume that the average IKE input by the wind is balanced by the turbulent dissipation in the boundary layer and radiation of NIWs. The averaged flux from the wind to ML inertial motions during CINDY is thus similar to the weaker, nonresonant, forcing events described in *Soares and Richards* [2013].

6. Near-Inertial Waves in the Pycnocline

Following the peak of the ML inertial oscillations, NIW packets are observed propagating downward in the pycnocline, as indicated by the slanted phase lines of meridional current upward-phase filtered current anomalies shown in Figure 9a. The packets are clearly defined in the band-passed near-inertial kinetic energy (KE) depth time-series plots (Figures 9c and 9d). The near-inertial band is defined here as the variability in the 2–6 days period, or roughly 0.6 $f_\circ$ −1.8 $f_\circ$. Three main packets are identified, termed from top down as WP1, WP2, and WP3 and centered at 65–70 m, 110–120 m, and 200–220 m, respectively (Figure 9d). Our ultimate goal is to derive their KE flux.

Rescaling the near-inertial currents with the Wentzel-Kramers-Brillouin (WKB) scale allows removal of the wave energy dependency on $N(z)$ (the resulting energy "correction" factor is $N_\circ/N(z)$) [*Sanford*, 1991; *Alford et al*., 2012]. The reference $N_\circ$ used for scaling is the average N beneath the TL, roughly between 80 and 500 m. Because of the rapid variation of N in the TL, depth bins inside the TL are stretched/shrunk assuming the TL N is constant. When plotted in WKB stretched depth [*Sanford*, 1991], WP1 and WP2 appear as part of the wake following the ML forcing event (Figure 9d). For WP3, its elevated energy density and timing of

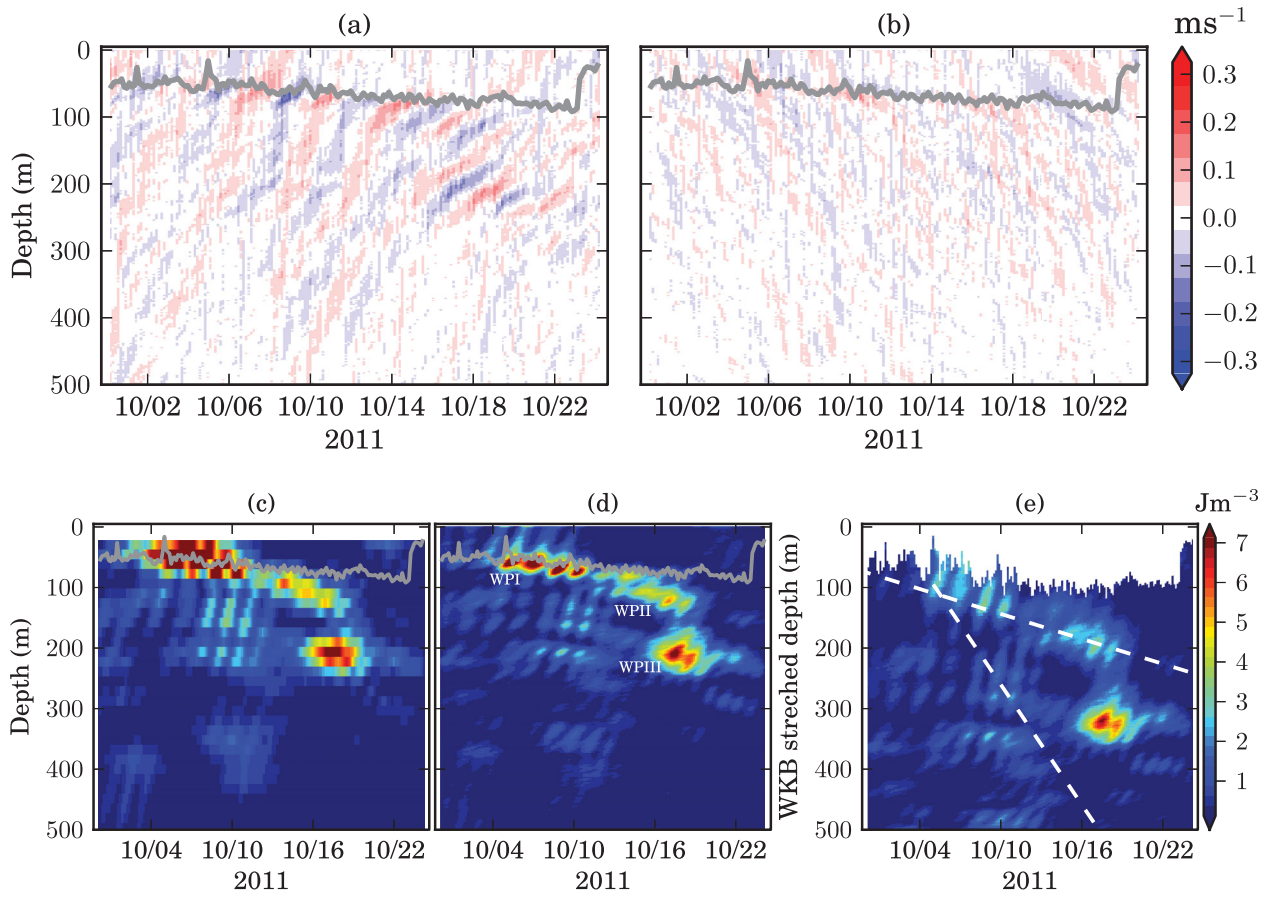

Figure 9. (top) Depth-time series of (a) upward phase (downward energy) propagating meridional velocity (v_{up}) and (b) downward phase (upward energy) propagating meridional velocity (v_{dn}) components from LADCP data. (bottom) Downward radiating near-inertial kinetic energy computed from 2–6 day band-passed current anomalies for (c) SADCP, (d) LADCP, and (e) LADCP but WKB scaled and plotted over WKB stretched depth. Wave packets of interest are labeled with white text as WP1, WP2, and WP3. The white-dashed lines denote ray paths, one forward ray path extrapolating WP1 using the wave packet method estimated c_{gz} and a backward ray path extrapolating the WP2 estimated c_{gz}.

arrival suggest that there must be another source of KE, or that this packet is exposed to different dynamics.

Because elevated turbulent kinetic energy dissipation rates were measured at the same time and depth of WP3 (the magenta box in Figure 3a), we calculate a diagnostic energy balance to estimate how much near-inertial KE was lost in this event (Section 6.5). This diagnostic is also used to estimate the relative contributions of the horizontal and vertical wave energy flux divergence, wave advection by background currents and dissipation along its propagation path, which is compared with a three-dimensional ray tracing exercise.

6.1. The Wave-Packet Method

The observed near-inertial signals are assumed to be plane waves with close neighboring frequencies and wavenumbers (i.e., narrow bandwidth) propagating in a slowly varying background field (the WKB approximation), superposing to form a packet or group. Under the assumptions that the background geostrophic flow is in solid body rotation and that its vertical shear, divergence and strain rates are negligible, the wave-packet theoretical framework allows combining direct estimates of wave frequency, propagation direction, vertical wavenumber, and energetics to derive an estimate of the f_{eff} felt by the wave packet and, with further information on the background geostrophic currents, of the wave's intrinsic frequency ω_i [*Alford and Gregg*, 2001].

The intrinsic frequency of a NIW packet, written as

$$\omega_i = \omega_\circ - |k_H||\mathbf{U}|\cos(\phi - \Theta), \tag{1}$$

is the frequency of a wave following the background motion, an important parameter for waves propagating in an inhomogeneous medium [see *Kunze*, 1985]. Conversely, the Eulerian frequency $\omega_\circ$, observed at a fixed location, is the intrinsic frequency ω_i plus the Doppler shift by the background currents **U**. In the above equation, k_H is the horizontal wavenumber, ϕ is the direction of wave propagation, and Θ is the direction of the background current. In this framework, the ratio of the wave's average KE to potential energy (PE) is proportional to the ratio of ω_i to f_{eff}, that is $r = \frac{\omega_i}{f_{\text{eff}}}$. Similarly, the major to minor axis ratio of a near-inertial current ellipse is also proportional to ω_i/f_{eff} (see Appendix A). As in *Alford and Gregg* [2001], we combine a simplified dispersion relation for internal waves propagating in a geostrophic sheared environment given by

$$\omega_i^2 = f_{\text{eff}}^2 + N^2\frac{k_H^2}{m_\circ^2}, \tag{2}$$

where N is the background buoyancy frequency and $m_\circ$ the vertical wavenumber, with (1) and $r = \frac{\omega_i}{f_{\text{eff}}}$ and obtain

$$f_{\text{eff}} = \frac{\omega_o}{r + \frac{m_\circ|\mathbf{U}|}{N}\cos(\phi - \Theta)\sqrt{r^2 - 1}}. \tag{3}$$

We then use the CINDY measurements and three methods to provide estimates for the parameters ω_o, ϕ, r, and $m_\circ$ to calculate f_{eff} via equation (3). The first method is based on the Fourier transform (FFT) rotary spectrum and coherency spectrum as in *Alford and Gregg* [2001], the second method uses the Wavelet transform (WLT) (as in *Cuypers et al*. [2013]), and the third is described in *Hebert and Moum* [1994] (hereafter referred as HM94). Each of these three methods pinpoints a peak or dominant Eulerian frequency $\omega_\circ$ and infers a wave propagation direction ϕ. There are two complimentary ways to infer this direction from single point depth-time series data. One is to use the phase relation between u_{up} and ρ_{up} denoted as ϕ_1 [*Alford and Gregg*, 2001]. The other is to use the tilt angle of the NIW current ellipse ϕ_2 (HM94), which tends to align with the direction of wave propagation. The peak frequency is then used to complex-demodulate the current and density time series to obtain estimates for r and $m_\circ$. We find the use of several methods useful because the short duration of the time series and intermittency of the NIWs yields poor spectral resolution and consequently lower statistical significance. Given the good agreement found between the three methods for frequency, for sake of brevity, we will show frequency results using the WLT only (Figure 10). A detailed step by step description of each method is in supporting information, and comparison of the different methods results can be found in supporting information figures.

To calculate (3), we use the cruise time-mean and linear trend in the current and stratification observations as background conditions. We then obtain ω_i from the definition of r and k_H by using (2). Our main interest is the vertical wave energy flux $F_z \approx c_{gz}\text{KE}^i$, where KE^i is the band-passed NIW kinetic energy and $c_{gz} = \frac{\omega_i^2 - f_{\text{eff}}^2}{m_\circ \omega_i}$. Note that, unlike the ML inertial oscillations, the solid body rotation approximation is essential to allow the calculation to work for the interior NIWs (cf. Appendix A) and, as discussed, this comes with significant overhead. Since we focus on the downward energy (upward phase) propagation, the first step prior to any of the analyses above is to use a two-dimensional (in time and depth) Fourier transform filter on the u, v, and ρ fields to separate signals with upward phase propagation (u_{up}, v_{up}, and ρ_{up}, respectively) from those with downward phase propagation, as shown in the top plots of Figure 9 for v. Because the SADCP and LADCP currents are in excellent agreement below the ML (e.g., compare Figures 9c and 9d), the analysis described here uses only LADCP. Some SADCP analysis is included in supporting information Figures S7 and S8.

6.2. Results of NIW Packet Analysis

From Figures 9a and 9b, one can see that the current anomalies with upward phase propagation dominate over the anomalies with downward phase propagation. No significant upward energy (downward phase) propagation is observed in association with the wave packets labeled in Figure 9d and the near-inertial band explains 60% of the variance of the upward phase currents. Two distinct stages of this response can

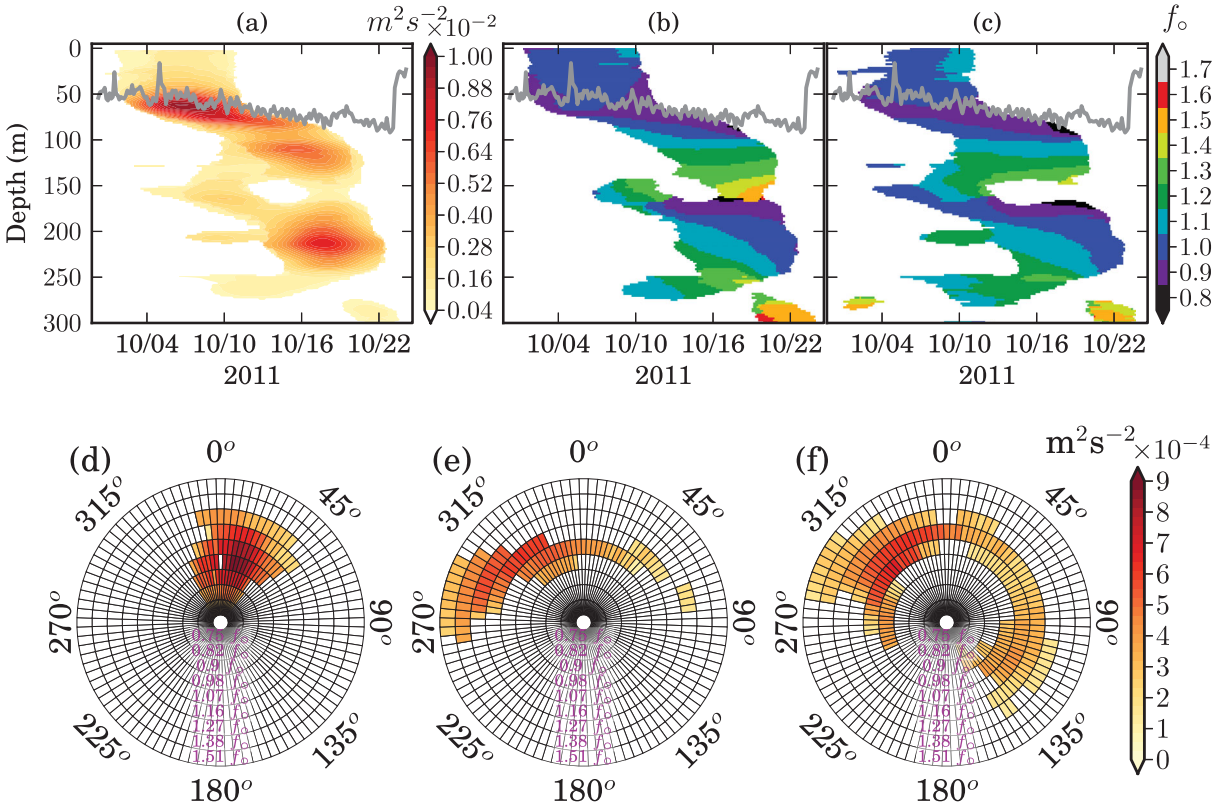

Figure 10. (a) Variance in the 2–6 days band from the Wavelet Transform (WLT) of LADCP currents with upward propagating phase. (b) Peak frequency in the WLT spectrum of u_{up}. (c) Peak frequency in the WLT spectrum of v_{up}. Directional spectrum of the NIW band obtained from the WTL coherence phase between u_{up} and ρ_{up} for (d) WP1 (60–90 m), (e) WP2 (110–140 m), and (f) WP3 (180–240 m). Angles denote direction waves propagate toward, with 0° being North. Bins along the radius show the frequencies in the 2–6 day band from low at the center to high at the edges. Filled bins are color-coded based on the u_{up} energy density. Only values coherent above the 95% significance level are shown.

be delimited: prior to and after 13 October. In both stages, a series of phase breaks in the top plots of Figure 9 indicates the distinctiveness of wave groups that constitute the field. Groups with low vertical wave numbers (e.g., WP1) dominate the first stage of the response while higher vertical wavenumbers dominate the second stage (e.g., WP2 and WP3). During the first stage, we also note near-inertial motions extending down to about 250 m, although these are less energetic than the signal in the TL associated with WP1.

Figures 10b and 10c show that the frequency increases with depth down to about 150 m, from slightly subinertial values near the base of the ML to about 12–30% superinertial. The WLT highlights that the subinertial frequencies dominate earlier in the record, immediately after the wind forcing event on 2 October (see Figures 10b and 10c and 4). The frequency increases with depth at progressively later times. WP1, therefore, is constituted by waves with subinertial frequencies occurring between ≈50 and 90 m, while WP2 is associated with the increasingly superinertial waves between ≈100 and 140 m. A sharp transition back to subinertial to inertial frequencies occurs around 150 m in all methods (Figures 10b and 10c and supporting information Figures S2a–S3a). Below 150 m, peak frequencies increase with depth again, albeit at a slightly slower rate (e.g., Figure 10b). The levels of constant frequency are tilted in (depth, time)-plane for WP3.

According to the directional spectra, WP1 (Figure 10d) propagates toward N-NE (20–40° true). The propagation direction ϕ_1 for WP2 veers northward then north-northwestward with depth (Figure 10e). WP3 propagates toward NW-N, although significant E-SE propagation is also found, particularly in the WLT analysis (Figure 10f). The southeastward waves dominate the 170–200 m depth bin, while the northwestward waves dominate below 200 m. The directional spectrum of both the FFT and WLT additionally indicates that the ESE propagating waves have subinertial and inertial frequencies, and that the superinertial waves propagate

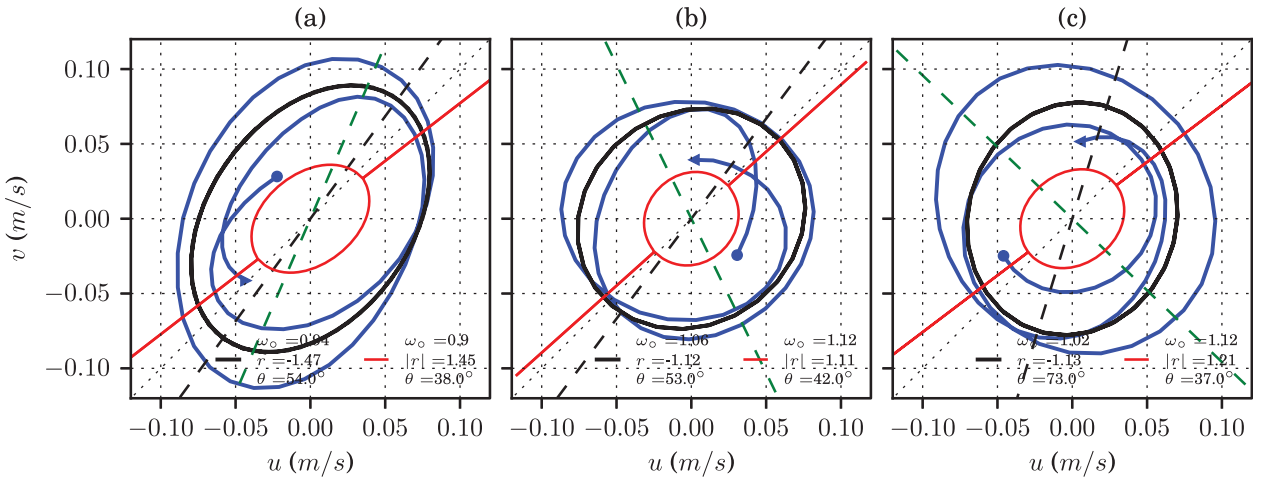

Figure 11. Near-Inertial ellipses computed from demodulated u_{up} and v_{up} at (a) 70 m using $\omega_\circ = 0.93 f_\circ$ (WP1), (b) at 113 m using $\omega_\circ = 1.12 f_\circ$ (WP2), (c) $\omega_\circ = 1.05 f_\circ$ at 216 m depth (WP3). Also shown are NIW ellipses obtained from FFT (red) and HM94 (black, dashed line shows the major axis) methods. Green-dashed lines show ϕ_1 obtained from the coherence spectra.

NW-ward. We note that an overlap of two such signals likely induces considerable uncertainties in the propagation direction ϕ_1 and ϕ_2 estimates for WP3.

The NIW current ellipses for each packet are plotted in Figure 11 and supporting information Figure S8. The ϕ_2 estimated with both the HM94 (Figure 11a, black line) and the FFT (Figure 11a, red line) methods agree quite well with ϕ_1 (Figure 11a, green dashed line) for WP1. Agreement is rather poor for WP2 and WP3, but blue curves in Figures 11b and 11c indicate that for WP2 and WP3, near-inertial currents do not trace a consistent ellipse over time. Instead, it appears that the ellipse tilt changes within the observation period. Hence, ϕ_1 estimates for WP2 and WP3 tend to agree with the orientation angle of near-inertial ellipses only when their amplitude is largest (Figures 11b and 11c).

The various methods used here suggest that the ratio $r = \omega_i / f_{\text{eff}}$ decreases with depth and time, along the propagation path of the NIW packets (Figure 12). Elongated near-inertial ellipses (Figure 11a) and lower ratios of wave $\overline{\text{KE}}$ to $\overline{\text{PE}}$ (from Figure 12b) support the high values of r (above 1.4, cf. quoted values in Figure 11) found in the TL, thus implying very superinertial intrinsic frequencies (relative to background f_{eff}) for WP1. The estimates derived from energy ratios, r_1, vary substantially over the WP1 period (Figure 12b), and are possibly impacted by the exchanges of *PE* between the TL and the ML, while the two estimates using NIW ellipse eccentricity, r_2, are more robust (Figure 12a). This robustness is afforded by the ellipses being tilted consistently.

In contrast, r estimates based either on eccentricity or energy ratios are in good agreement for WP2 (Figure 12), despite ellipse tilts not agreeing very well with the propagation direction from the coherence spectrum ϕ_1 (Figure 11b). Calculations indicate a substantial reduction in r associated with WP2, implying superinertial intrinsic frequencies ≈10% above f_{eff}. This reduction in r can be at least partially explained by the Doppler shift as discussed below. Increases in r below 135 m occur concomitantly with increases in $\omega_\circ$, however, the confidence level at these depths is much lower.

Waves in WP3 appear to behave more inertially than in WP2 (Figure 12b). The HM94 method suggests a minimum r_1 value near unity (Figure 12a), implying no wave propagation. Beneath ≈150 m, however, energy ratio and ellipse eccentricity estimates of r start to diverge: while energy ratios computed using the HM94 technique and WLT suggest a significant reduction in r_1 for WP3 in relation to WP2, ellipse eccentricities obtained either with the FFT or HM94 methods, as well as energy ratios calculated using the FFT peak frequency (instead of the WLT), produce similar r_2 values between WP3 and WP2 (Figure 12a), i.e., superinertial like. The near-inertial current ellipses traced by demodulated currents (Figure 11c, blue curve) seem to corroborate a wave with superinertial intrinsic frequency and propagation axis oriented NW-SE, although the SADCP demodulated currents show a more circular pattern (supporting information Figure S8c). A close

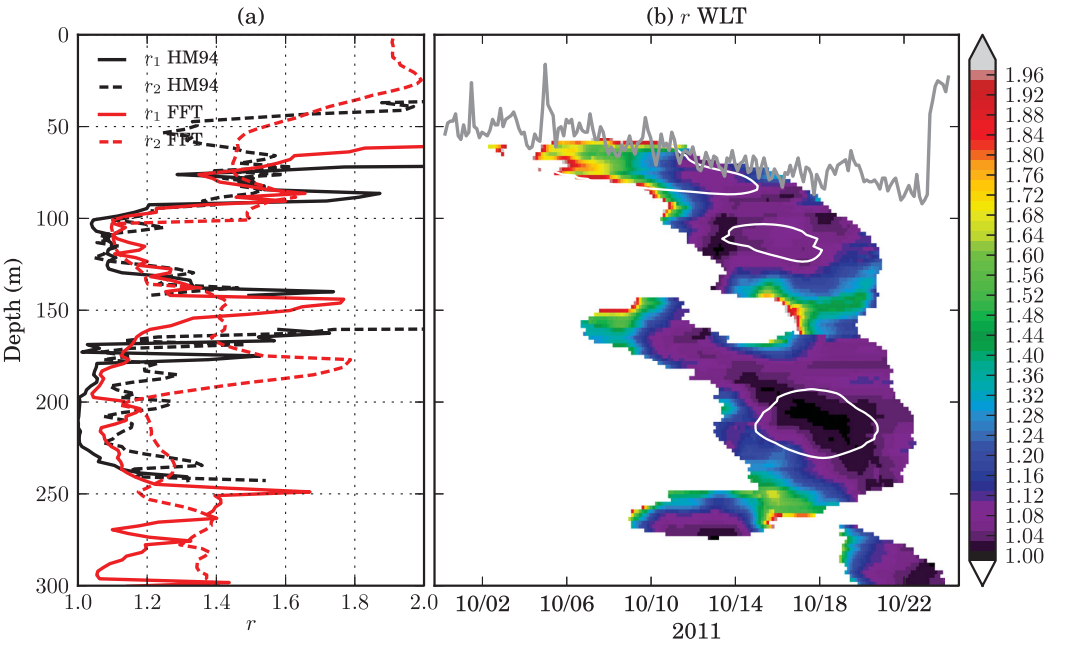

Figure 12. (a) Profiles for r_1 and r_2 using different methods. Note that the FFT gives an average representation of the whole time series for a given frequency, at a given depth, while the HM94 method describes an average behavior within a narrower interval in the time series, at a given depth. (b) r_1 at every time instance and depth using its primary WLT frequency. White contours denote regions of high NIW variance.

inspection of Figure 12b indicates that high r_1 occur mostly above 200 m, and perhaps slightly later than the r_1 minimum, and appear associated with the E-SE subinertial signal, suggesting that these are the waves with superinertial intrinsic frequency.

Estimates for the vertical wavenumber $m_\circ$ are compiled in Figure 13. As noted in the beginning of this section, NIWs observed prior to 13 October typically have low wavenumbers, roughly in the range 0.02–0.04 rad m^{-1} or 300–150 m wavelength, while NIWs observed after 13 October display higher wavenumbers, in the range 0.04–0.07 rad m^{-1} (e.g., Figure 13b). Figure 13b also suggests that $m_\circ$ tends to increase with both depth and time for waves within WP2 and WP3. Note that these values are given in WKB-stretched meters. For comparison, Figure 13a shows vertical wavenumbers estimated with the HM94 method in WKB stretched meters, as well as in nonstretched depth as one would typically observe (black-dashed line). This comparison reveals the refraction pattern of the NIWs induced by $N(z)$: in normal depth WP2 and WP3 have similar vertical scales, however this occurs because of elevated stratification (Figure 3e) in WP2 relative to WP3. The TL stratification causes the same effect in WP1 waves. WKB-stretching allows a clearer separation of wave packets, indicating a decrease in vertical scale from WP1 to WP3 likely driven by the background flow, as discussed below. Note that here, the WKB scaling and stretching is an arbitrary change of coordinate with no dynamical implications and thus no impact on the subsequent calculations. As an independent check of the HM94 method, we plot two vertical wavenumber spectra for upward-phase currents in Figure 13c, calculated and averaged for the first (blue curve) and second stages (green curve), showing peaks at 0.024, 0.043, and 0.08 rad m^{-1}, in good agreement with the nonstretched HM94 method.

Next we apply the various wave property estimates in equation (3) to calculate f_{eff} and the remaining wave properties. We discard wave properties estimated outside the depth and time (for WLT based) limits specified for each wave packet, where there is low signal to noise ratio. Assuming wave properties do not vary significantly over a couple of wave periods and within the depth range of a packet, weighted averages of wave properties are computed for WP1, WP2, and WP3 using weights given by the near-inertial variance (c.f. Figure 10a). The most likely value of wave properties, for each wave packet, is taken as the median of the various method's weighted averages. They are reported in Table 1, alongside an estimated likely range based on the 95% limits of the distribution function of the property in question, considering all estimates within the packet's depth-time bin and from all different methods. The choice to report these extremes as

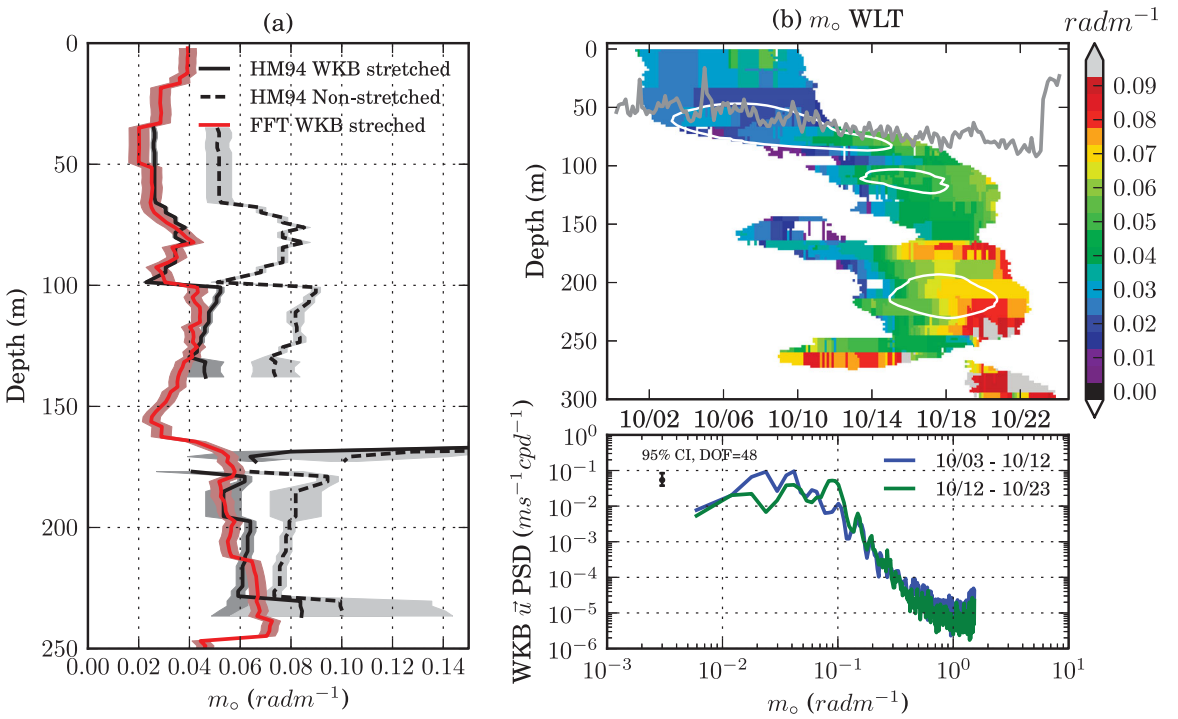

Figure 13. Estimates of NIW vertical wavenumber $m_\circ$. (a) WKB stretched $m_\circ$ profiles using peak frequencies from the HM94 method (blue curve) and the FFT spectrum (red curve), note that these profiles follow the times where NIW energy is significant. (b) WKB stretched $m_\circ$ based on demodulation with WLT peak frequencies. (c) Nonstretched vertical wavenumber spectrum for WKB-scaled currents, note the prominent peaks at wavenumbers consistent with nonstretched HM94 analysis in Figure 13a, viz., 0.024, 0.043, and 0.08–0.09.

the likely range for properties stems from the fact that variations in property are often larger along the vertical direction than between methods, probably reflecting the influence of different signals within a wave packet, as well as the changing background. Comparing most likely values for the different methods allows identification of biases or other systematic errors inherent in some of these methods, such that outliers are not considered in Table 1, see the Appendix A for a brief discussion of possible sources of error.

6.3. Inferred Refraction and Propagation Patterns

WP1 is the most energetic during the first stage of the response. Waves are observed with subinertial frequencies of about 0.93 $f_\circ$ and to propagate toward N-NE. Ellipse and energy ratios indicate very superinertial intrinsic frequencies of ≈1.46 $f_\circ$. This is consistent with NIWs propagating against the background geostrophic currents, which are toward WSW, within a highly stratified TL and within a region of anticyclonic vorticity, as suggested by the low value of f_{eff} in Table 1. Waves also appear to have shorter vertical scales (≈120 m) relative to the weaker near-inertial signals observed deeper in the water column caused by refraction in the TL. After WKB stretching, waves display lower vertical wavenumbers—longer vertical scales of about 215 m—in closer agreement with the weak signals below the TL. Notwithstanding large contamination in the estimates of r_1 and r_2 or deviations of the circulation from a state of solid body rotation, the horizontal wavelength is about 100 km. The superinertial character of WP1 implies downward group speeds of 20 m per day (33 in stretched depth), yielding a $\overline{\text{KE}}$ flux of ≈0.6 mWm^{-2}, with maximum flux as high as 1.7 mWm^{-2}.

WP2 appears in the second stage of the response, indicating the occurrence of energetic NIW over three IPs after the ML IKE peak. Incoming waves mostly propagate toward N-NW and superinertial frequencies are observed to arrive as the near-inertial signal deepens (e.g., Figures 10b and 10c). WP2 is entering a region of slightly weaker background stratification in relation to WP1, and where background currents veer W-NW, such that the waves are now propagating with the background flow. Therefore, estimated WKB stretched vertical wavenumbers show a decrease in vertical scale relative to WP1 driven by the changes in the

Table 1. Summary Table of Wave Properties[a]

NIW Property	WP1 (50–90 m)	WP2 (100–140 m)	WP3 (175–245 m)
$\omega_\circ$ ($f_\circ$)	0.93, 0.90–0.96	1.13, 1.0–1.24	0.98, 0.92–1.04 and 1.05, 0.98–1.16
ϕ_1 (°True)	25, 0–36	336, 305–36	127, 0–150 and 338, 0–300
ϕ_2 (°True)	37, 10–45	46, 4–129	16[b], 0–120
r_1	1.62, 1.18–2.51	1.13, 1.07–1.33	1.08, 1.06–1.15 and 1.03, 1.0–1.14
r_2	1.47, 1.25–1.63	1.16, 1.05–1.39	1.18, 1.08–1.29 and 1.15, 1.07–1.29
λ_z[c] (m)	216, 150–260	143, 120–180	102, 75–118
f_{eff} ($f_\circ$)	0.75, 0.66–0.88	0.85, 0.74–1.02	1.14, 1.06–1.39 and 0.90, 71–1.03
ω_i ($f_\circ$)	1.06, 1.0–1.3	0.94, 0.86–1.16	1.24, 1.04–1.54 and 0.96,.78–1.06
λ_H (km)	107, 69–142	138, 62–190	100, 58–140 and 480, 120–1900
c_{gz}[c] (m d^{-1})	33, 25–42	7, 4–13	5, 3–12 and 2.5, 0–6
c_{gH}[c] (ms^{-1})	0.19, 0.13–0.28	0.07, 0.05–0.12	0.05, 0.035–0.12 and 0.04, 0–0.07
F_z (mWm^{-2})	0.61, 0.29–0.83	0.12, 0.06–0.28	0.08, 0.04–0.27 and 0.08, 0–0.20

[a]Most likely value, followed by range.
[b]Ellipse orientation does not display bimodal distribution.
[c]Values in WKB stretched meters.

background flow, with a negative Doppler shift reducing the intrinsic frequency, as evidenced by the lower r_1 and r_2 values. The r values are consistently around 1.12 down to 125 m depth (Figure 12) despite the rapidly increasing $\omega_\circ$. Because the background-current vertical shear therein is very weak, this r value can only be maintained by a positive $f_{\mathrm{eff}}/f_\circ$ gradient. In agreement with NIWs of reduced intrinsic frequency, estimated horizontal wavelengths are longer for waves in WP2 at ≈140 km, and have slower downward group velocities and weaker energy fluxes compared to WP1. Below 130 m, both $\omega_\circ$ and r increase rapidly and the waves appear to propagate more westward which would result in an increased Doppler shift, and so a strong reduction in the required f_{eff} gradient to counter its effects, but as already mentioned, these are weak, low confidence signals.

WP3 is highly energetic despite being located well below the main pycnocline (Figure 9c). In spite of larger uncertainties in the analysis of this packet, the bimodal distribution of wave properties (except the high vertical wavenumber) hints at the presence of two distinct wave groups within the 70 m depth range where this packet is observed. A group with subinertial to inertial $\omega_\circ$ and S-ESE propagation dominates signals above 200 m, albeit at lower significance levels, while below 200 m the dominant group has inertial to superinertial $\omega_\circ$ and NW-NNW propagation. The WKB stretched vertical wavenumber $m_\circ$ associated with both groups is further reduced relative to WP2 and WP1, again implying that gradients in background vorticity and/or flow offset the effects of the weakening stratification. The low $\omega_\circ$ group appears to have high intrinsic frequency relative to the local effective inertial frequency, while the high $\omega_\circ$ group appears to behave inertially (low r, Figure 12). The Doppler shift raises ω_i above $\omega_\circ$ and lowers ω_i below $\omega_\circ$ for the subinertial group and the superinertial group, respectively (Table 1).

Since the background currents remain west-northwestward, it is unlikely that Doppler shift gradients alone explain all observed refraction. The combined evidence, therefore, suggests that waves are propagating into higher $f_{\mathrm{eff}}/f_\circ$ relative to WP2, specifically in what is now an environment with cyclonic vorticity (Table 1). The analysis further suggests that the northward superinertial NIWs are approaching a critical level or Rossby singular level [*Kunze*, 1985; *Wurtele et al*., 1996], resulting in inertial-like intrinsic frequency, decreasing (increasing) vertical (horizontal) scale, near zero vertical group speeds and energy flux and the energy levels well above expected. In this scenario, the subinertial southward signal could be explained by waves that have been reflected from a turning point or singularity located somewhere downstream.

The scenario described above suggests that the NIWs propagate downward into an increasingly cyclonic environment, i.e., where $f_{\mathrm{eff}}/f_\circ$ increases with depth (Table 1). An independent check for these f_{eff} estimates is made by comparisons to MERCATOR f_{eff}. The blue curves in Figure 14a show MERCATOR cruise period averaged f_{eff} depth profiles at the sampling station and at several locations within a 1° radius of the station. The model relative vorticity switches from anticyclonic to cyclonic between 100 and 250 m, in qualitative agreement with the pattern proposed by the wave packet analysis. This reversal is also observed in instantaneous model outputs during the cruise period (solid lines in Figure 6).

The magnitudes of f_{eff} from MERCATOR however are significantly lower than estimated from observations (regardless of the averaging timescale), particularly those associated with WP1, as AVISO and OSCAR were found to be for the ML estimates (see Section 5). The bias toward higher $|f_{\mathrm{eff}}|$ in the analysis may imply that

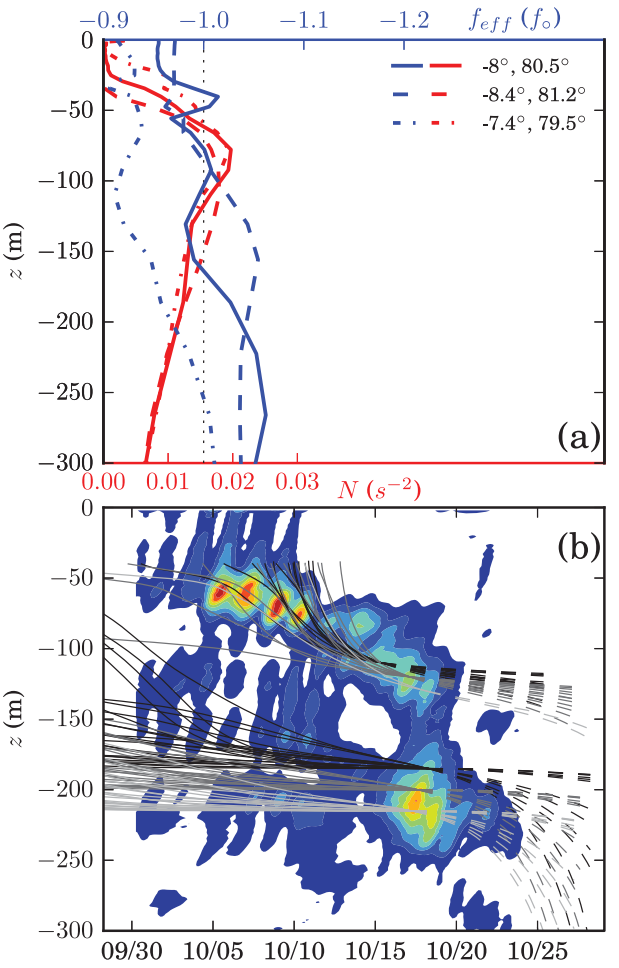

Figure 14. (a) MERCATOR N (red curves) and f_{eff} (blue curves) profiles at the locations marked in Figure 16. (b) Ray depths for WP2 and WP3 backtracked to the base of ML (solid lines) and forward traced for 15 days (dashed lines). Each line represents a different initial wavenumber and lighter shades of gray denote rays with a deeper starting depth. For reference, the color contours show the near-inertial kinetic energy from LADCP measurements.

the background circulation may not be in solid body rotation (see section 5 and Appendix A). In fact, if a packet with the same ω_i and r as WP1 was propagating in a background parallel shear flow, the f_{eff} estimate would be reduced to 0.87 $f_\circ$, a value in closer agreement with both model output and the ML inertial oscillation frequency. Another source of bias is baroclinicity in the background flow, which is significant for WP1 (see the Appendix A). The negative cross-propagation background current shear (background currents veer WNW from SW with depth, see Figure 5a), given WP1 propagates toward NNE, raises r (and ω_i as well). When corrected, WP1 f_{eff} then becomes 0.89 $f_\circ$, in better agreement with MERCATOR. This bias may have a significant impact in second order estimates k_H, c_{gz} and F_z, and therefore we believe that the lower bounds of these estimates are more likely to be true.

Uncertainty in most wave property estimates shown in Table 1 tend be narrower for WP1 because all methods (Figures 10b and 10c, supporting information S2a and S3a) consistently point to a dominant subinertial frequency and the same direction of propagations throughout the WP1 period and depth interval. In WP1, the main source of uncertainty lies in the large differences between r_1 and r_2 estimates. Such large differences between r_1 and r_2 are not observed for WP2 and may be due to contamination in near-inertial $\overline{PE}$ from ML entrainment and detrainment driven by boundary layer processes. Therefore, we deem r_2 more reliable for WP1, although WP1 may also be affected by the Ekman currents in similar manner as the ML inertial oscillations. For WP2 and WP3, rather than r, uncertainties in wave property estimates stem from the difficulty in establishing a dominant signal because of the fast changes in peak frequency $\omega_\circ$ with depth, while the larger uncertainties in the various estimates for WP3 stem from additional difficulty in establishing reliable direction (ϕ) estimates. The time series collected during CINDY is about seven inertial periods (IP) long, and NIW packets are present only for a small fraction of time (typically 2 IPs), which makes determining a peak frequency and direction very challenging due to frequency resolution issues. In spite of these limitations, sensitivity experiments do show that r and $m_\circ$ estimates display little sensitivity to the particular choice of peak frequency as long as the $\omega_\circ$ used for demodulation are within two or three $\Delta\omega_\circ$, the typical FFT frequency resolution.

In a time invariant background flow, $\omega_\circ$ is constant, making it reasonable to expect that the measured $\omega_\circ$ at CINDY is the frequency at which waves were generated. The $\omega_\circ$ increase with depth describes the dispersal characteristics of packets: either the separation rate of an initial broadband packet starting at a single location or arrivals of multiple, different narrowband packets generated at ever poleward locations. We interpret the CINDY observations as the arrivals of internal swells generated further "upstream," as in *Qi et al.* [1995]. Thereby, WP1 is composed of fast propagating NIWs generated by the event in the vicinity of the CINDY

station, while WP2 are NIWs still forced by the same event, but somewhere southeastward of the R/V *Mirai* location (likely near 9°S). This is consistent with the increase in $\omega_\circ$ and the veering of ϕ_1 toward N-NW with depth. The backward extrapolated ray trajectory for WP2 (dashed white lines in Figure 9e) suggests it could have indeed been generated by this same forcing event, although details will require taking into account the vertically varying background flow. Depending on how horizontally homogeneous the forcing and background conditions were, it is possible to interpret our point observations as representative of what occurs along a wave ray path.

WP3 however defies such simple interpretation, not only because of difficulties in pinpointing a dominant frequency and direction, but because it arrives earlier than would be expected from a ray trajectory starting at the base of the ML in the beginning of the cruise and passing through WP1 and WP2. WP3 could have been generated by an earlier wind event. The CCMP wind record shows an event in the region 35 days before the CINDY cruise, which would require an average c_{gz} of -5 m/d. If generated by the same event though, WP3 would need to follow a different trajectory than WP2 and originate at a different location (closer to the station than WP2, given WP3 lower $\omega_\circ$).

Ray trajectories from simple extrapolation of the WP1 c_{gz} estimates of Table 1 (Figure 9e) suggest that the unlabeled energy (Figures 9c and 9d) and anomalies (Figures 9a and 9b) observed before 13 October, between 90 and 250 m, could also be part of the near-inertial wake from the wind bursts. Close inspection shows waves with similar propagation direction (toward NNE), superinertial Eulerian frequencies (e.g., $\omega_\circ \approx 1.05 - 1.24\ f_\circ$), and high r. Similarly to WP1, the WKB vertical wavenumber of these disturbances is in the low range and given their propagation heading, likely originate southwest of the station. Dominance of anticyclonic vorticity in the upper 200 m prior to and during the early sampling period (dark-grey line in Figure 6) could allow such a fast downward route assuming these conditions are also prevalent up-wave-trajectory, even though their propagation heading implies a weakened Doppler shift since the background flow below the TL is northwestward (assuming that is also the case up-wave-trajectory).

6.4. Ray Tracing

We use three-dimensional (3-D) ray tracing to investigate whether WP2 can be traced back to a nearby southeast location, within a time matching the wind forcing as hypothesized, and whether it is reasonable to assume that the observed differences between WP1 and WP2 represent wavenumber variations along a ray trajectory. We also evaluate whether rays encounter singularities (such as critical levels) or turning points. The ray equations and algorithm are based on *Kunze* [1985] and are described in supporting information.

Rays are traced backward and forward in a time invariant background stratification and circulation taken from MERCATOR output time averaged between 1 and 25 October. An ensemble of initial ray conditions for position and wavenumber (k, ℓ and m) for WP2 and WP3 are extracted from Table 1: three values for vertical and horizontal wavenumbers, spanning the range of likely values, while several propagation directions are chosen depending on the packet. Four rays are initiated at three different starting depths set in accordance to the depth span of each observed wave packet (e.g., WP2 has rays seeded at 110, 120, and 130 m). Initially, the four rays form a regular tetrahedron. The four rays are then traced together, and changes in the tetrahedron volume provide an estimate of energy density changes due to ray divergence (see supporting information). Note that vertical wavenumbers are adjusted from WKB values to unstretched depth coordinates using the model $N(z)$ profiles (Figure 14a) for dynamical consistency. Of the approximately hundred ray tubes started at a given location, only a subset of the ray tubes that have an r value consistent with those derived from the observations is shown.

Several ray tubes representing WP2 were seeded at the location of the CINDY station (8°S 80.5°E) and traced back in time for 25 days or until rays reach the base of the ML, taken as 40 m deep everywhere. The time and depth evolution of a subset of these rays is shown in Figure 14b by solid lines. Most rays reach the base of the ML in 5–10 days (Figure 14b) somewhere southeast of CINDY (Figure 16). Various wave properties and the background f_{eff} along track are shown in Figure 15. The wave characteristics near the ML base are in good agreement with what would be expected from observed WP1 properties, i.e., the high ω_i/f_{eff} and higher horizontal wavenumbers than initialized with (this can also be seen in Figure 16). However, the hindcast wave direction at generation is westward rather than the observed NNE. The hindcast vertical

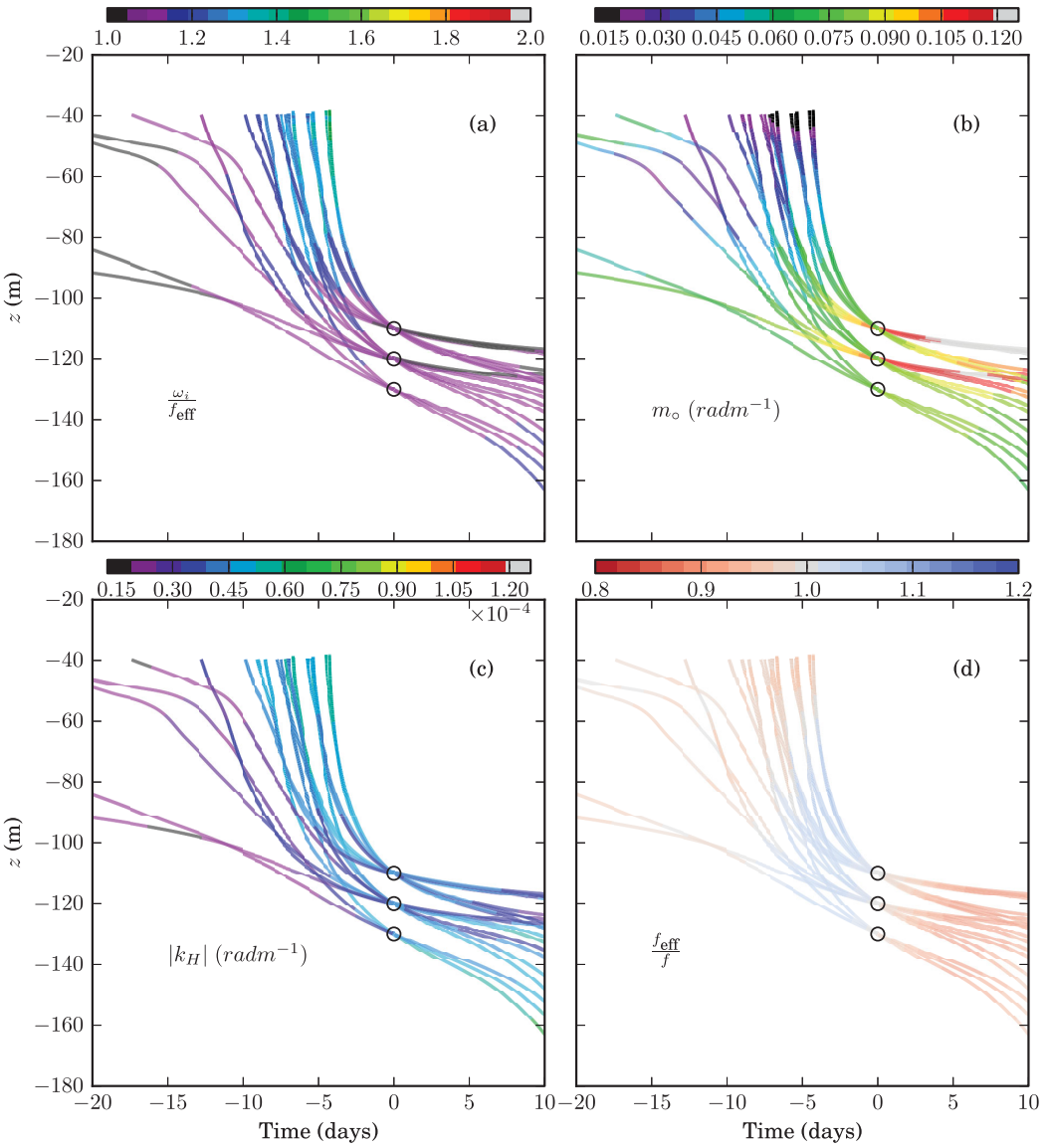

Figure 15. Properties for select WP2 rays backward and forward traced from the CINDY station: (a) ω_i/f_{eff} (r), (b) vertical wavenumber $m_\circ$, (c) horizontal wave number $|k_H|$, (d) background f_{eff}/f. Approach to critical layer are indicated by $\omega_i/f_{\text{eff}} \rightarrow 1.0$ and $m_\circ \rightarrow \infty$. Circles denote the starting points.

wavenumber (Figure 15b) decreases as waves back-propagate into a relatively less stratified upper pycnocline to the southeast (see dashed red line in Figure 14a). The very low values of *m* near the ML base occur because of wave propagation into the zone of decreasing stratification (e.g., above the *N* maximum, see Figure 14a) due to the absence of a strongly stratified TL in MERCATOR. As waves approach this *N* maximum, ray convergence leads to an increase in energy density (reduced volume, third column of Figure 16), when waves propagate past the *N* maximum *m* decreases and volume increases again.

WP3 rays were also back-traced for 25 days. A larger number of rays were seeded at the station location, spanning both SE and NNW signal characteristics. They also are shown in Figure 14b (horizontal maps can be found in supporting information). Rays with southeast propagation and superinertial intrinsic frequencies though, did not yield numerical stable results and are not shown. Nonetheless, only a few of the rays propagate above 150 m. Even rays with relatively high ω_i/f_{eff} do not propagate more than 20 m upward. This occurs because WP3 is initialized within a cyclonic vorticity layer with mean currents directed toward

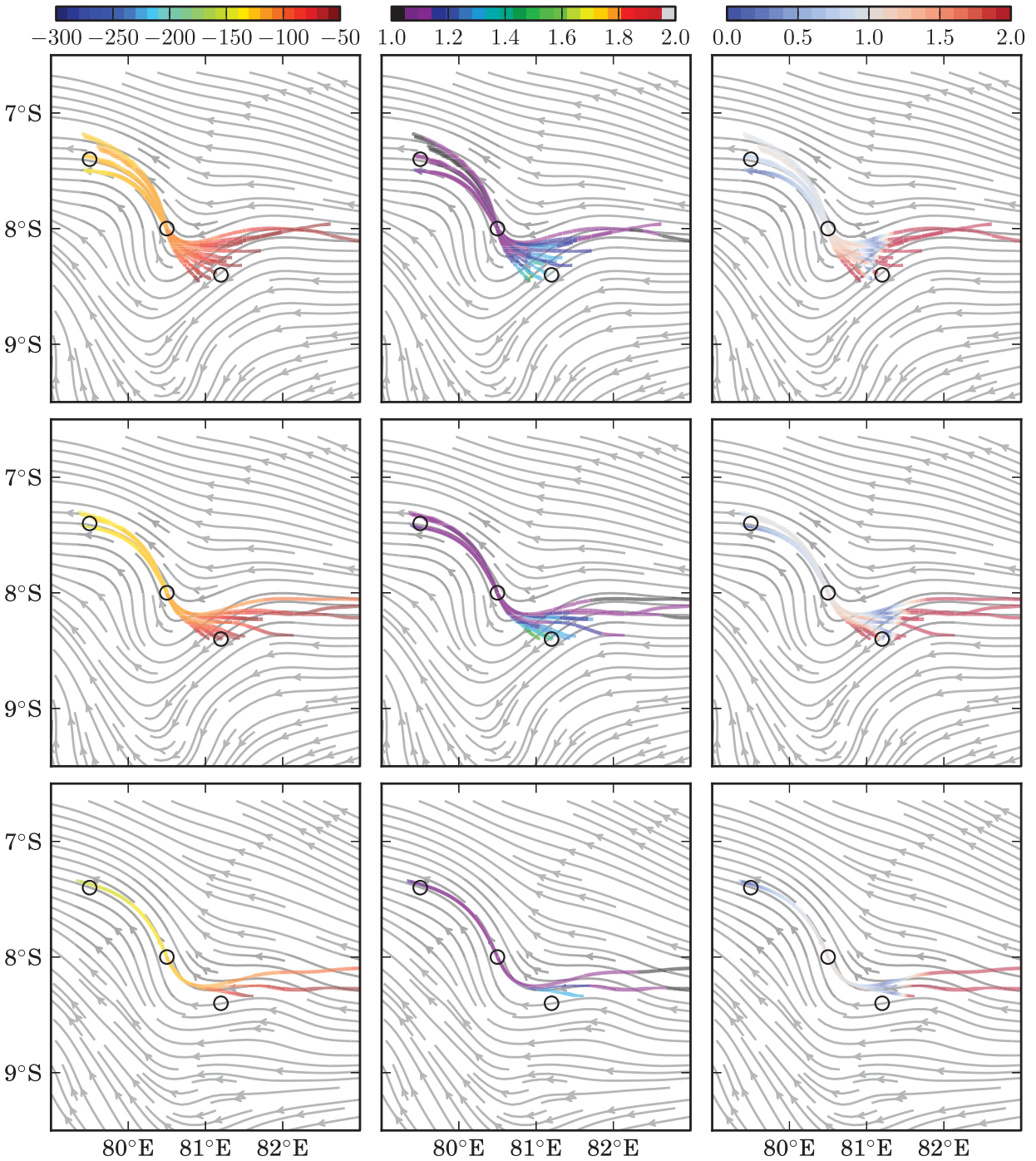

Figure 16. Maps for WP2 rays backward and forward traced from the CINDY station starting at 110 m (top row), at 120 m (middle row), and 130 m (bottom row). Rays are color coded by depth in meters (first column), the ratio ω_i/f_{eff} (second column), and the ray tube volume relative to its initial volume (third column). Streamlines show the background circulation at the starting depth. Black circles mark the locations where profiles of background N and f_{eff} are extracted.

NW (e.g., various f_{eff} profiles in Figure 14a) which effectively traps rays within it, e.g., waves that would be approaching from the top refract away from this layer because of the increase in f_{eff} and negative Doppler shift. When WP3 rays are traced forward in time (dashed lines in Figure 14b), wave depth penetration is limited for the initially inertial like groups.

These results are in agreement with an experiment where WP2 rays are forward traced starting from the CINDY station. Several of the ray trajectories (dashed lines in Figure 14b) show that ray depth penetration plateaus. Rays tend to become more inertial like (Figure 15a) and the vertical wavenumber increases (Figure 15b), thereby greatly reducing the vertical group speed. Reductions in ray tetrahedron volume (Figure 16 third column) indicate that ray convergence is occurring, implying an increase in wave energy density. These characteristics are usually associated with a critical level or Rossby singularity [e.g., *Lighthill*, 1978; *Wurtele et al*., 1996]. The energetics near this singular level is explored in the next section. We highlight that the singular behavior is also brought about by the propagation into a WNW jet, suggesting that depth-dependent Doppler shifting, not only vertical gradients of f_{eff}, plays a key role in setting up this process. Even though propagation is reduced to a halt, waves are still advected toward the NW (Figure 16) and may resume propagation downward if conditions become favorable again.

This exercise has taken the WKB approximation beyond its limits of formal validity and should be viewed with caution. Nonetheless, we consider the results of 3-D ray tracing qualitatively consistent with the scenario proposed in the previous section, at least in supporting the plausibility that the observed NIW packets: (i) were generated by the same wind bursts of the beginning of the sampling period, though at different locations and thus reaching the fixed point station by different paths; (ii) exhibit a refraction pattern consistent with the approach to a critical level. The results of Figure 15 generally support the notion that the local observations of WP1 and WP2 represent the refraction pattern along a ray, although some details do not match well with the wave-packet analysis results. Furthermore, advection and the Doppler shift play a prominent role on the dynamics of the NIWs investigated here, such that the critical level discussed here is essentially different than the one of *Kunze et al*. [1995] because WP3 is not trapped within a well-defined feature due to vorticity. Ray tracing experiments where the Doppler shift term is omitted show much slower NIW depth penetration than when background vorticity is removed (see experiments reported in supporting information Figure S10).

We could not determine a source for WP3 by backward tracing. We investigate if a fast downward route could exist by running additional experiments where rays with WP1 characteristics are forward traced downward from the TL for 25 days, starting at various geographical points. Overall, the results were consistent with the previous experiments, for most rays initiated in the immediate vicinity of the station veer northwestward and decrease their intrinsic frequency with depth (supporting information Figure S9). Rays seeded directly south of the station penetrate into the pycnocline much faster and turn southeast (though not involving singular behavior) when approaching the station, suggesting that it is at least possible that WP3 could originate from the same event.

The discrepancies between the ray tracing model and observations may be attributed to uncertainties in initial ray conditions and/or an oversimplified choice background field (time frozen, model derived). On the former, note that backward WP2 rays initiated with a low aspect ratio reach the surface slightly sooner than the peak of the forcing, suggesting that the high horizontal wavenumbers quoted in Table 1 are overestimated. Regarding the latter, it is seems likely that the model cyclonic layer is shallower than in reality, given that rays typically do not reach 150 m. Experiments with background fields derived from different averaging periods and timescales produce similar results. A background field slowly evolving in time may be needed for a more accurate ray evolution and to better explain our observations.

6.5. Wave Energy Budget

We investigate the mechanisms responsible for the observed NIW energy patterns by estimating terms in the KE balance for NIWs in an inhomogeneous background. The goal is not to provide a closed energy budget, but rather, as in *Hebert and Moum* [1994] to try and diagnose the relative importance of the terms. From the conservation of wave action, an equation for the energy density for NIWs (E^i) in a background flow, $\mathbf{U}$, can be written as

$$\frac{\partial E^i}{\partial t}+\nabla_H\cdot\mathbf{F}_H+\frac{\partial F_z}{\partial z}+\mathbf{U}\cdot\nabla E^i+E^i\nabla\cdot\mathbf{U}=\epsilon+B+\frac{E^i}{\omega_i}\frac{d\omega_i}{dt}+I, \tag{4}$$

where $\frac{d}{dt}=\frac{\partial}{\partial t}+\left(\mathbf{c}_g+\mathbf{U}\right)\cdot\nabla$, ϵ is the turbulent dissipation of wave energy (the measured ϵ times ρ), B represents energy lost to mixing via buoyancy flux, I represents wave-wave and wave-turbulence interactions [*Kunze et al*., 1995] and the subscript H denotes only horizontal components are retained. In this study, E^i is

Table 2. Energy Budget Terms in mWm^{-2}

	$\frac{\partial}{\partial t}\int KE dz$[a]	$\overline{\int \epsilon + B dz}$	$\overline{F_z^B - F_z^T}$	R	$\overline{\frac{KE}{\omega_i}\frac{d\omega_i}{dt}}$
WP1−WP2 65–130 m	−0.003	−0.10 (−0.13)	0.24 (0.16)	0.14 (0.06)	−0.012

[a] $\bar{x} = 1/T \int x dt$, where T is the period between WP1 and WP2. $\overline{\int \epsilon + B dz}$ in parenthesis are calculated without subtraction of the constant dissipation rate, see text for details. $\overline{F_z^B - F_z^T}$ in parenthesis are calculated from the lower bounds shown in Table 1.

approximated by KE^i, B is taken as $\gamma\epsilon$, with $\gamma = 0.2$ being a typical coefficient for mixing efficiency [*Hebert and Moum*, 1994]. The term $\frac{E^i}{\omega_i}\frac{d\omega_i}{dt}$, represents wave energy exchanged with the background [*Kunze et al*., 1995; *Chavanne et al*., 2010]. Following *Hebert and Moum* [1994]; *Kunze et al*. [1995], I is set to zero. We return to this approximation as it pertains to WP3 later. From Figure 6b, another reasonable approximation is $E^i \nabla \cdot \mathbf{U} = 0$.

Using the measured currents and the outputs of the linear wave analysis (Table 1), a simplified and depth integrated version of equation (4) can be calculated:

$$\frac{\partial}{\partial t}\int E^i dz = \left(F_z^T - F_z^B\right) - \int (1.0+\gamma)\epsilon dz + R, \tag{5}$$

where F_z^T and F_z^B are the NIW energy flux at the top and bottom limits of a control volume, and R is the vertical flux residual. The depth integration is performed between WP1 and WP2 (60–130 m) and for WP3 (between 175 and 245 m, see magenta box in Figure 3b). The terms in (5) are shown as averages over an integration period, corresponding to 14.25 days between WP1 and WP2.

The LHS and the second term in the RHS of (5) are calculated directly from the measurements, where KE^i is taken from the 2–6 days band-passed upward-phase LADCP currents, while ϵ is taken from the MSP measurements reduced by a constant dissipation rate associated with other processes (as in *Hebert and Moum* [1994]). The value for this constant is calculated as the mean dissipation over the time series, and reduces the measured dissipation rate by 30%. The first term on the RHS of (5) is the net flux of KE^i into the control volume and is calculated using the results in Table 1, which represent the average wave flux over ≈2 IPs and so reduced over the integration period. We treat WP3 differently (see below) because of a difficulty in defining boundaries for the net vertical flux calculation due to the lack of a clear propagation signal connecting WP1 and WP3.

The vertical flux residual R is then assumed to represent the combined effects of horizontal flux divergence, horizontal advection and energy exchange with the background:

$$R = -\int \left(\mathbf{U} + \mathbf{c}_{gH}\right) \cdot \nabla_H E^i - E^i \nabla_H \cdot \mathbf{c}_{gH} + \frac{E^i}{\omega_i}\frac{d\omega_i}{dt} dz. \tag{6}$$

Note that in this expression, the horizontal energy flux divergence is separated into the ray convergence term and the x advection term. An indirect estimate for the wave-mean flow exchange term can be derived from ω_i values in Table 1 as well, if it is assumed that changes from WP1 to WP2 and WP3 represent conditions along rays, a reasonable assumption for WP1-WP2 based on the ray tracing experiments done in the previous section, less so for WP1-WP3. Estimating the remaining terms, given only point observations, is impossible as they require information over at least a wavelength distance or quantifications done along a ray (i.e., Lagrangian).

The size of the different terms in equation (5) is summarized in Table 2. It can be seen that the net vertical energy flux is the largest term, while the time change of energy is negligible within the periods considered in the calculation. No significant sensitivity of these results to changes in the integration period was found. Between WP1 and WP2, the turbulent dissipation and mixing are expected to account for about 40% loss, leaving a substantial positive residual flux that must be balanced out by wave propagation or sinks. Because the intrinsic frequency in the WP1-WP2 ray decreases as it propagates, energy is lost to the background flow [*Kunze*, 1985; *Chavanne et al*., 2010], however the contribution of this term is estimated to be small, of the order of 10% of the dissipation, in agreement with *Kunze et al*. [1995]. Since ray tracing suggests that rays converge onto the station, implying an increase in energy density, lateral wave propagation and advection by the mean flow must account for most of the energy loss. Unfortunately, the contribution of ray

convergence could not be quantified at this stage. The significant residual, however, agrees with the ray tracing results showing continuous wave advection beyond the sampling station.

To account for the possibility that wave fluxes are overestimated, these calculations are repeated using net flux into control volumes based on lower bounds of F_z from Table 1 (values in the parenthesis of Table 2). This obviously reduces the size of the residual, but shows that a nonnegligible amount of energy must still be propagated or advected laterally. Also shown in parenthesis are quoted values for the average dissipation and mixing if the full measured dissipation rates were used, showing that there is ample dissipation to balance the NIW vertical flux.

For WP3, an even simpler version of equation (5) is calculated within the magenta box shown in Figure 3b by integrating energy density, its rate of change and the measured TKE dissipation between 175 and 245 m from 15 October 15 to 22 October (Figure 17). During the integration period, KE^i rises and falls (black curve), yielding a small net energy gain of about 0.01 kJm^{-2} during this period. The energy rise is attributed to the propagation and convergence of NIW energy into the site, while part of the energy loss is accounted for by the local dissipation (shown in red, integrates to 0.08 kJm^{-2} in the period). The dissipation rate peaks with the energy density, and the measured dissipation removes about 20% of the peak observed energy. Despite the relatively high dissipation rates, it is clear that a large residual is present throughout the period (e.g., blue curve minus red curve), resulting in a net energy excess $\int Rdt$ of $\approx$ 0.09 kJm^{-2} that needs to be accounted for by wave propagation, advection, and convergence. This residual translates into a net wave energy flux out the box of about 0.15 mWm^{-2}. Given that WP3 is approaching its inertial, nonpropagating limit, this residual is most likely accounted for by the background flow advection, which moves wave energy out of our study site.

The diagnostic employed demonstrates that dissipation is an important term in the action balance throughout a NIW life cycle, from ML base to down into the pycnocline, typically accounting for at least 50% of the largest estimated term: the net vertical input from wave flux. The data also indicate a single dissipation event in the pycnocline may remove 15–25% of the peak NIW energy, implying that the NIW packet was not completely dissipated. As hypothesized by *Kunze et al*. [1995], interaction of NIWs with the background flow is estimated to be only about 10% of dissipation. In contrast to those authors, horizontal advection by mean flow and/or wave propagation accounts for at least 30–50% of the observed reduction in energy. Therefore, lateral processes may be an essential component in the dynamics of these observations, in agreement with the ray tracing results showing ray energy reaching well beyond the station (Figures 16). In other words, the CINDY NIWs are likely not trapped within a well-defined mesoscale feature, in contrast to the observations of *Kunze et al*. [1995].

We believe the dissipation event was directly induced by NIWs approaching a Rossby singularity. For instance, *Wurtele et al*. [1996] found that inertia-gravity waves approaching such singularities can produce reflections of higher harmonics of the incident waves due to nonlinearity, if the incident inertia-gravity wave has a fairly monochromatic spectrum. Although the wave-packet analysis suggests two distinct signals in WP3, the data does not show any clear evidence of reflecting waves (high wave number, upward energy, downward phase waves), at least nothing that stands out from the background. In this budget, wave-wave interactions were neglected ($l = 0$), yet as discussed by *Kunze et al*. [1995], they can be an important mechanism to transfer NIW energy to smaller scales where dissipation is more effective, which is of particular importance within the TL where fine-scale shear may not be sufficiently strong to overcome the stratification. Conditions for wave-wave interactions such as random superpositioning of NIW packets were not explored here.

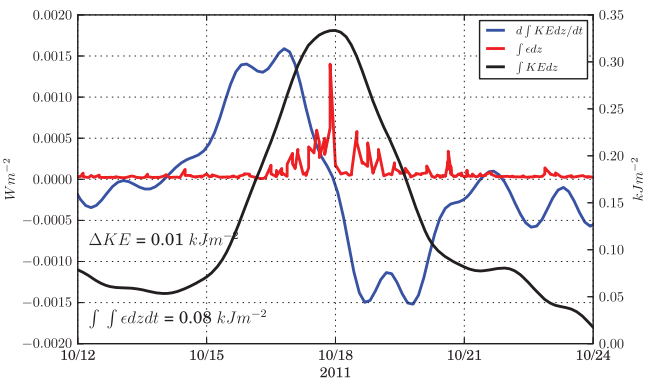

Figure 17. Time series of energy balance terms for WP3, depth integrated between 170 and 245 m. The left axis is for fluxes (local rate of change of kinetic energy and turbulent kinetic energy dissipation ϵ, blue and red line, respectively), while the right axis is for kinetic energy density. Quoted values denote quantities time integrated between 15 October and 22 October.

7. Conclusions and Discussion

Near-inertial waves observed in the tropical Indian Ocean were examined using a suite of methods based on linear plane wave dynamics. The data show three distinct wave packets propagating downward in the pycnocline after the excitation of ML inertial oscillations by a series of wind pulses at the beginning of a fixed-station time series. These wind pulses are linked to the developing stages of an MJO event [*Gottschalck et al*., 2013]. We estimate that the upper most NIW packets carry 30–40% of the average wind input of IKE to the ML. Consistent with this picture, the observed near-inertial kinetic energy integrated in the pycnocline is roughly one third of the ML IKE. The above fraction is substantially higher than global average near-inertial radiation predicted by numerical models [*Furuichi et al*., 2008], and is at the upper limit of estimates by *Alford et al*. [2012] for Station Papa in the midlatitude Pacific. Our result is consistent with recent work by *Soares and Richards* [2013] suggesting elevated rates of NIW radiation in tropical regions, as well as with other observational studies in midlatitudes showing significant NIW energy at and below the seasonal pycnocline [*Alford*, 2010; *Alford et al*., 2012].

We attempted to convey the difficulties in ascertaining the precision and accuracy of these flux estimates. Rather than relying on standard significance tests from statistical techniques, emphasis is put on discussing the impacts of the various assumptions made in order to compute the estimates. In particular, the WKB approximation is employed to obtain various wave parameters and interpret the results. This assumption warrants some a posteriori justification. The approximation is valid when the wave scale is smaller than the scale on which the wavenumber varies [*Gill*, 1982] and, based on the observed change in vertical wavelength between WP1 and WP2, this is well satisfied. Nonetheless, we provide several qualitative checks and indirect evidence to lend further confidence to our interpretations, using large ensemble ray tracing and a comparison with model output when appropriate. Agreement with previous work is particularly encouraging. The most challenging aspects of this analysis stem from the lack of data on the horizontal structure of the NIW field and background conditions. As a suggestion, future field campaigns targeting similar phenomena should include focus on collecting data on the spatial structure, perhaps using glider missions in conjunction with mooring arrays. Although NIWs are also present in the MERCATOR output, the lack of vertical resolution in the thermocline means the NIW packets are not adequately resolved and precludes a useful comparison with our observations.

The most likely scenario is that NIW energy propagates ≈200 m into the pycnocline within 5 IPs. In the upper 100 m this quick propagation is primarily driven by the baroclinic structure of the background flow, via the Doppler shift term, rather than the background vorticity. Our analysis also suggests that the NIWs propagate in an inhomogeneous background circulation favoring the occurrence of a critical level around the deepest observed NIW packet (WP3), via a dynamical combination of Doppler-shift effects and vertical gradients of vorticity. Elevated turbulent kinetic energy dissipation rates were measured in association with this wave packet and the possible critical layer. About 20% of the NIW energy is estimated to be lost in this single dissipation event. Furthermore, dissipation of wave energy is found to be an important energy sink as waves propagate through the pycnocline. Unlike previous observations within mesoscale eddies [*Kunze et al*., 1995] though, the NIWs in the CINDY observations do not appear trapped, and lateral fluxes are expected to play a significant role.

Assuming a mixing efficiency coefficient γ of 0.2, the vertical diffusion coefficient can be estimated as $\kappa_v = \gamma\epsilon/N^2$. The average κ_v associated with WP3 is $0.5–1\times10^{-4}\mathrm{m}^2\mathrm{s}^{-1}$, with spikes of 10^{-3}. Given that the observed strong dissipation event occurred over approximately 2 IPs, a decay timescale for NIW energy would then be about 40 days. Assuming all observed wave packets were generated around 2 October, the life cycle of NIWs could be ≈2 months. One may speculate, that if NIW energy contributes quite efficiently (e.g., 20%) to diapycnal mixing, 5–10% (30–40% × 20%) of the wind work on ML inertial oscillations is used to mix the ocean interior over a period of a couple of months. The above assumes a succession of similar dissipation events occurred outside the site. Further extrapolation of the NIW energy dissipation pattern derived from these observations would suggest that near-inertial energy is likely removed within the pycnocline, over a depth range of 200–500 m, effectively away from the abyssal ocean as suggested by e.g., *Zhai et al*. [2009].

Our study demonstrates that modest wind forcing may produce a significant wave field response, which in turn may lead to intense episodical mixing in an otherwise quiet pycnocline. By quantifying the energetics

associated with this far-field response, we have provided information to elaborate meaningful leading order parameterizations of NIW mixing for OGCMs. The potential impacts or feedbacks to longer timescales of these mixing episodes remain to be discovered.

Appendix A: NIW Polarization Relations

We briefly describe the linear polarization relations for NIWs and discuss how the assumptions impact the accuracy of the methods employed. *Kunze* [1985]'s set of equations (1) describes inviscid, unforced, linearized Boussinesq, and incompressible motions in a quasigeostrophic background flow whose vertical velocity is small enough to be negligible in the advective terms. Utilizing the hydrostatic approximation and a plane-wave solution of the form

$$(u', v', w', \rho', p') = (\hat{u}, \hat{v}, \hat{w}, \hat{\rho}, \hat{p}) \exp i(kx + \ell y + mz - \omega_\circ t), \tag{A1}$$

where the prime quantities denote wave motions and the hat quantities their respective complex amplitude, k, ℓ, and m the zonal, meridional, and vertical wavenumbers and $\omega_\circ$ the Eulerian frequency, Kunze's set of equations, after rotating the horizontal coordinates in the direction of wave propagation k, reduces to

$$\begin{aligned}
(-i\omega_i + U^r_{x^r})\hat{u^r} - (f - U^r_{y^r})\hat{v^r} + U^r_z \hat{w} &= -i\frac{k^r}{\rho_\circ}\hat{p} \\
(-i\omega_i + V^r_{y^r})\hat{v^r} + (f + V^r_{x^r})\hat{u^r} + V^r_z \hat{w} &= 0 \\
i\frac{m}{\rho_\circ}\hat{p} &= -\frac{g}{\rho_\circ}\hat{\rho} \\
k^r \hat{u^r} &= -m\hat{w} \\
-i\omega_i \hat{\rho} - fV^r_z \frac{\rho_\circ}{g}\hat{u^r} + fU^r_z \frac{\rho_\circ}{g}\hat{v^r} - \frac{\rho_\circ}{g}N^2\hat{w} &= 0.
\end{aligned} \tag{A2}$$

In the set (A2), ω_i is the intrinsic frequency (i.e., the frequency of a wave in a coordinate system following the background flow, see section 6.1), the superscript r denotes rotated quantities, $U^r_{x^r}$ and $U^r_{y^r}$ are the gradients of the along-propagation component of the background flow U^r in the along propagation axis (x^r) and the cross propagation axis (y^r), respectively. Likewise $V^r_{x^r}$ and $V^r_{y^r}$ are the gradients of the cross-propagation component of the background flow V^r. The determinant of (A2) yields a dispersion relation for NIWs, as well as the definition for an effective inertial frequency f_{eff} which incorporates the effects of the background vorticity and strain rate on the inertial frequency f, viz.,

$$f_{\text{eff}} = f\sqrt{1 + \frac{\zeta}{f} + \frac{1}{f^2}\left(\frac{\zeta^2 - S_n^2 - S_s^2}{4}\right)} \tag{A3}$$

where $\zeta = V^r_{x^r} - U^r_{y^r}$ is the vorticity, $S_n = U^r_{x^r} - V^r_{y^r}$ is the normal strain rate, and $S_s = V^r_{x^r} + U^r_{y^r}$ is the shear strain rate. It is also useful to introduce divergence $\delta = U^r_{x^r} + V^r_{y^r}$, and to note that these quantities have the same form in both rotated and nonrotated coordinates (i.e., rotationally invariant).

Polarization relations for u' and v' in terms of ρ' for NIW perturbations have complex amplitudes of the form

$$\hat{u^r} = i\frac{g\omega_i}{N^2}\frac{m}{k_H}\frac{\hat{\rho}}{\rho_\circ}, \tag{A4}$$

$$\hat{v^r} = \frac{g\omega_i}{N^2}\frac{m}{k_H}\frac{\hat{\rho}}{\rho_\circ}\frac{(f + V^r_{x^r})}{(\omega_i + iV^r_{y^r})}. \tag{A5}$$

To obtain equations (A4) and (A5), it was necessary to make the assumption that V^r_z and U^r_z are negligible, i.e., no baroclinicity in the background flow. See below for discussion of this approximation.

The kinetic-to-potential energy ratio is then

$$R=\frac{\overline{KE}}{\overline{PE}}=\frac{\omega_i^2}{N^2}\frac{m^2}{k_H^2}\left[1+\frac{(f+V_{x^r}^r)^2}{\omega_i^2+(V_{y^r}^r)^2}\right], \tag{A6}$$

where overbars denote averaging over a wave period and/or wavelength. It follows that R is not exactly proportional to ω_i/f_{eff} (as in *Alford and Gregg* [2001]), but is "contaminated" by the presence of background shears related to divergence and strain rates (namely $V_{y^r}^r$). In order to obtain the useful statement $r=\omega_i/f_{\text{eff}}=\sqrt{\frac{R+1}{R-1}}$ of *Alford and Gregg* [2001], two additional simplifications to equation (A6) are required: (i) $V_{y^r}^r$ must be negligible as well as δ and S_n, and (ii) the background flow must be either in solid body rotation such that $U_{y^r}^r=-V_{x^r}^r$, allowing to set $f_{\text{eff}}^2=(f+V_{x^r}^r)^2$. In parallel shear flow background, equation (A6) remains valid but $\sqrt{\frac{R+1}{R-1}}\neq\frac{\omega_i}{f_{\text{eff}}}$, rendering the analysis impossible. These assumptions are harder to justify. Divergence indeed appears to be small (Figure 6b), however several strain components are of similar magnitude to vorticity (Figures 6c and 6d). Solid body rotation or parallel shear flow are unlikely to dominate in a geostrophic turbulent scenario suggested by OSCAR/AVISO or MERCATOR output (Figure 7).

The phase relations between u' and ρ' are also impacted by the presence of background shears. After rotating back to earth coordinates, polarization relations for the above are expressed as:

$$u'=\frac{g\omega_i}{N^2}\frac{m}{k_H}\frac{\hat{\rho}}{\rho_\circ}\left[i\cos\phi^E-\frac{f+V_{x^r}^r}{\omega_i+iV_{y^r}^r}\sin\phi^E\right]\exp(i\varphi), \tag{A7}$$

$$\rho'=\hat{\rho}\exp(i\varphi). \tag{A8}$$

Where $\varphi=kx+\ell y+mz-\omega_i t$ is the wave phase and ϕ^E is the horizontal direction of wave propagation in degrees counterclockwise from East. In order for the lead/lag between u' and ρ' to accurately represent the wave propagation direction in degrees true ϕ, besides the approximations mentioned in the previous paragraph, it is also required that $\omega_i\rightarrow f_{\text{eff}}$ (assuming $f_{\text{eff}}=f+V_{x^r}^r$). This way, equation (A7) when in the south hemisphere reduces to:

$$u'=\frac{g\omega_i}{N^2}\frac{m}{k_H}\frac{\hat{\rho}}{\rho_\circ}\exp(i\varphi+\phi), \tag{A9}$$

where now a phase lead or lag ϕ in u' over ρ' is equal to the horizontal wave-propagation direction in degrees true.

From set (A2), the u' to v' polarization relation can be written as

$$\frac{\hat{u}}{\hat{v}}=\frac{-i\omega_i+V_y+\tan\phi_2^E\left(f-U_y+\ell m^{-1}U_z-km^{-1}V_z\right)}{\tan\phi_2^E(-i\omega_i+U_x-km^{-1}U_z)-(f+V_x)+km^{-1}V_z}. \tag{A10}$$

Equation (A10) shows that NIW currents draw an ellipse with tilt generally aligned with the propagation direction axis, ϕ_2^E, but with modifications by the background current shears. Considering our estimates of the aspect ratio of NIWs, the terms regarding the influence of vertical background shears are in general small, except in the TL where they are of the same order (i.e., 10% $f_\circ$) as the horizontal shears, and are neglected here, at the expense of accuracy, only to permit the analysis. The ratio of major to minor axis, or its eccentricity, after rotating the complex amplitudes by ϕ_2^E is then:

$$\frac{\hat{u}_r}{\hat{v}^r}=\frac{-i\omega_i+V_{y^r}^r}{-(f+V_{x^r}^r)}. \tag{A11}$$

From the above equation, it is clear that the imaginary component of the ratio $r_2=\hat{u}_r/\hat{v}_r$ is proportional to $\omega_i/(f+V_{x^r}^r)$ and the real part proportional to $V_{y^r}^r/(f+V_{x^r}^r)$. An easier ratio to measure (e.g., from the FFT rotary spectrum) would be:

$$|r_2|^2=\frac{V_{y^r}^{r^2}}{(f+V_{x^r}^r)^2}+\frac{\omega_i^2}{(f+V_{x^r}^r)^2} \tag{A12}$$

Again, it is obvious the necessary approximations $V^r_{y^r}=0$ and of solid body rotation for $r_2=\omega_i/f_{\text{eff}}$. We note that the first approximation above is of tolerable consequence for background horizontal shears order 10% of $f_\circ$, with its direct impact on r_2 (and r_1) of a few percent at most. Nonetheless, in order to estimate r_2, one needs to rotate the wave currents by ϕ_2, which is difficult to back out from the observed ellipse since its tilt is affected by the background shears as well. For a 10% $f_\circ$ $V^r_{y^r}$, the tilt angle is modified by about 10°. Effectively any estimate of r_2 is contaminated with this uncertainty in ϕ_2 determination.

Acknowledgments

We thank the CINDY2011 project Principal Investigators and personnel, its funding agency, the Japan Agency for Marine-Earth Science and Technology (JAMSTEC) and in particular, the captain, crew, and technicians of the R/V Mirai. Financial support from NOAA (through grant NA13OAR4310168) is gratefully acknowledged, as well the Coordenação de Aperfeiçoamento de Pessoal de Nível Superior (CAPES) and the Fulbright program for partially funding S. M. Soares. The CINDY cruise data can be found at http://www.jamstec.go.jp/iorgc/cindy/obs/obs.html. OLR imagery provided by NCAR/EOL under sponsorship of the National Science Foundation and downloaded from http://apdrc.soest.hawaii.edu/datadoc/noaaolr_daily.php. CCMP Wind data are produced by PODAAC (https://podaac.jpl.nasa.gov/Cross-Calibrated_Multi-Platform_OceanSurface-WindVectorAnalyses) and downloaded from http://apdrc.soest.hawaii.edu/datadoc/ccmp_6hourly.php. AVISO data are available at http://www.aviso.altimetry.fr/duacs/and OSCAR data can be found at http://www.oscar.noaa.gov/index.html. MERCATOR OCEAN global analysis is graciously provided by Mercator Océan of France, http://www.mercator-ocean.fr. We also thank the two anonymous reviewers for their valuable comments.

References

Alford, M. (2003), Improved global maps and 54-year history of wind-work on ocean inertial motions, *Geophys. Res. Lett.*, *30*(8), 1424, doi: 10.1029/2002GLO16614.

Alford, M. H. (2001), Internal swell generation: The spatial distribution of energy flux from the wind to mixed layer near-inertial motions, *J. Phys. Oceanogr.*, *31*, 2359–2368.

Alford, M. H. (2010), Sustained, full-water-column observations of internal waves and mixing near mendocino escarpment, *J. Phys. Oceanogr.*, *40*(12), 2643–2660.

Alford, M. H., and M. C. Gregg (2001), Near-inertial mixing: Modulation of shear, strain and microstructure at low latitude, *J. Geophys. Res.*, *106*(C8), 16,947–16,968.

Alford, M. H., M. F. Cronin, and J. M. Klymak (2012), Annual cycle and depth penetration of wind-generated near-inertial internal waves at ocean station papa in the northeast Pacific, *J. Phys. Oceanogr.*, *42*(6), 889–909.

Atlas, R., R. N. Hoffman, J. Ardizzone, S. M. Leidner, J. C. Jusem, D. K. Smith, and D. Gombos (2011), A cross-calibrated, multiplatform ocean surface wind velocity product for meteorological and oceanographic applications, *Bull. Am. Meteorol. Soc.*, *92*(2), 157–174.

Bonjean, F., and G. S. Lagerloef (2002), Diagnostic model and analysis of the surface currents in the tropical Pacific ocean, *J. Phys. Oceanogr.*, *32*(10), 2938–2954.

Chavanne, C., P. Flament, G. Carter, M. Merrifield, D. Luther, E. Zaron, and K. Gurgel (2010), The surface expression of semidiurnal internal tides near a strong source at Hawaii. Part I: Observations and numerical predictions*, *J. Phys. Oceanogr.*, *40*(6), 1155–1179.

Chavanne, C. P., E. Firing, and F. Ascani (2012), Inertial oscillations in geostrophic flow: Is the inertial frequency shifted by $\zeta/2$ or by ζ?, *J. Phys. Oceanogr.*, *42*(5), 884–888.

Cuypers, Y., X. Le Vaillant, P. Bouruet-Aubertot, J. Vialard, and M. J. Mcphaden (2013), Tropical storm-induced near-inertial internal waves during the Cirene experiment: Energy fluxes and impact on vertical mixing, *J. Geophys. Res. Oceans*, *118*, 358–380, doi:10.1029/2012JC007881.

D'Asaro, E. (1985), The energy flux from the wind to near-inertial motions in the surface mixed layer, *J. Phys. Oceanogr.*, *15*(8), 1043–1059.

D'Asaro, E. (1989), The decay of wind-forced mixed layer inertial oscillations due to the β effect, *J. Geophys. Res.*, *94*(C2), 2045–2056.

Dohan, K., and R. E. Davis (2011), Mixing in the transition layer during two storm events, *J. Phys. Oceanogr.*, *41*(1), 42–66.

Fairall, C., E. Bradley, J. Hare, A. Grachev, and J. Edson (2003), Bulk parameterization of air-sea fluxes: Updates and verification for the coare algorithm, *J. Clim.*, *16*(4), 571–591.

Furuichi, N., T. Hibiya, and Y. Niwa (2008), Model-predicted distribution of wind-induced internal wave energy in the world's oceans, *J. Geophys. Res*, *113*, C09034, doi:10.1029/2008JC004768.

Gill, A. E. (1982), *Atmosphere-Ocean Dynamics*, 662 pp., Academic, San Diego.

Gottschalck, J., P. E. Roundy, C. J. Schreck III, A. Vintzileos, and C. Zhang (2013), Large-scale atmospheric and oceanic conditions during the 2011–12 DYNAMO field campaign, *Mon. Weather Rev.*, *141*(12), 4173–4196.

Hebert, D., and J. Moum (1994), Decay of a near-inertial wave, *J. Phys. Oceanogr.*, *24*(11), 2334–2351.

Jiang, J., Y. Lu, and W. Perrie (2005), Estimating the energy flux from the wind to ocean inertial motions: The sensitivity to surface wind fields, *Geophys. Res. Lett.*, *32*, L15610, doi:10.1029/2005GL023289.

Jochum, M., B. P. Briegleb, G. Danabasoglu, W. G. Large, N. J. Norton, S. R. Jayne, M. H. Alford, and F. O. Bryan (2013), The impact of oceanic near-inertial waves on climate, *J. Clim.*, *26*(9), 2833–2844.

Kunze, E. (1985), Near-inertial wave propagation in geostrophic shear, *J. Phys. Oceanogr.*, *15*(5), 544–565.

Kunze, E., R. W. Schmitt, and J. M. Toole (1995), The energy balance in a warm-core ring's near-inertial critical layer, *J. Phys. Oceanogr.*, *25*(5), 942–957.

Lighthill, J. (1978), *Waves in Fluids*, Cambridge University Press, Cambridge, U. K.

Plueddemann, A., and J. Farrar (2006), Observations and models of the energy flux from the wind to mixed-layer inertial currents, *Deep Sea Res. Part II*, *53*(1-2), 5–30.

Pollard, R., and R. Millard Jr. (1970), Comparison between observed and simulated wind-generated inertial oscillations, *Deep Sea Res. Oceanogr. Abstr.*, *17* 813–816.

Qi, H., R. A. De Szoeke, C. A. Paulson, and C. C. Eriksen (1995), The structure of near-inertial waves during ocean storms, *J. Phys. Oceanogr.*, *25*(11), 2853–2871.

Sanford, T. B. (1991), Spatial structure of thermocline, abyssal internal waves, in *Dynamics of Oceanic Internal Gravity Waves, Proceedings of the 6thAha Hulikoa Hawaiian Winter Workshop*, edited by P. Muller, pp. 109–141, Publication Services, SOEST, Honolulu.

Seiki, A., M. Katsumata, T. Horii, T. Hasegawa, K. J. Richards, K. Yoneyama, and R. Shirooka (2013), Abrupt cooling associated with the oceanic Rossby wave and lateral advection during cindy2011, *J. Geophys. Res. Oceans*, *118*, 5523–5535, doi:10.1002/jgrc.20381.

Shinoda, T., T. G. Jensen, M. Flatau, S. Chen, W. Han, and C. Wang (2013), Large-scale oceanic variability associated with the Madden-Julian oscillation during the CINDY/DYNAMO field campaign from satellite observations, *Remote Sens.*, *5*(5), 2072–2092.

Soares, S., and K. Richards (2013), Radiation of inertial kinetic energy as near-inertial waves forced by tropical Pacific easterly waves, *Geophys. Res. Lett.*, *40*, 1760–1765, doi:10.1002/grl.50387.

Watanabe, M., and T. Hibiya (2002), Global estimates of the wind-induced energy flux to inertial motions in the surface mixed layer, *Geophys. Res. Lett.*, *29*(8), 1239, doi:10.1029/2001GL014422.

Wurtele, M., A. Datta, and R. Sharman (1996), The propagation of gravity-inertia waves and lee waves under a critical level, *J. Atmos. Sci.*, *53*(11), 1505–1523.

Yoneyama, K., C. Zhang, and C. N. Long (2013), Tracking pulses of the Madden-Julian oscillation, *Bull. Am. Meteorol. Soc.*, *94*(12), 1871–1891.

Zhai, X., R. Greatbatch, C. Eden, and T. Hibiya (2009), On the loss of wind-induced near-inertial energy to turbulent mixing in the upper ocean, *J. Phys. Oceanogr.*, *39*(11), 3040–3045.